UNIVERSITY OF TARTU
Faculty of Science and Technology
Institute of Chemistry

Ekaterina Pozdnyakova

Pyrolytic Metamorphosis of Zn-TAL MOF into Highly Active Nitrogen-Doped Carbon Catalyst for Oxygen Reduction Reaction

Bachelor's Thesis (12 ECTS)

Curriculum Science and Technology

Supervisors:
Akmal Kosimov, Ph.D
Nadežda Kongi, Ph.D

Tartu 2025

Pyrolytic Metamorphosis of Zn-TAL MOF into Highly Active Nitrogen-Doped Carbon Catalyst for Oxygen Reduction Reaction

Abstract:

Metal-organic frameworks (MOFs) are promising precursors for the synthesis of high-performance metal-nitrogen-carbon (M-N-C) electrocatalysts. However, during pyrolysis, MOF's initial structure integrity often breaks down and yields catalytically inactive metal agglomerates. This study describes the pyrolytic conversion of a Zn-MOF to Zn-N-C electrocatalyst. The optimized pyrolysis of the Zn-TAL MOF precursor successfully preserved its hollow sphere morphology, while the relatively low boiling point of zinc prevented the formation of Zn agglomerates. The pyrolysis at 1000 °C yielded ZnMOF-1000 - a highly porous electrocatalyst (S_{BET} = 615 m^2 g^{-1}) with excellent oxygen reduction reaction (ORR) performance, namely onset potential (E_{onset}) value of 0.98 V, and half-wafe potential ($E_{1/2}$) value of 0.84 V vs. reversible hydrogen electrode (RHE), comparable to the commercial Pt/C electrocatalyst. physical characterisation was performed to assess the morphology of the carbon framework, the absence of zinc aggregates, and the composition of the catalyst. In an anion exchange membrane fuel cell (AEMFC), the ZnMOF-1000 reached a peak power density of 553 mW cm^{-2} at 60 °C. The results show that Zn-TAL MOF is a promising precursor for Zn-N-C catalysts, offering an efficient platinum-free electrocatalyst option for fuel cells.

Keywords:

Oxygen Reduction Reaction (ORR), Electrochemistry, Metal-Organic Frameworks (MOFs), Nitrogen-Doped Carbon Catalyst

CERCS: P395 Organometallic chemistry, P400 Physical chemistry, P401 Electrochemistry

Zn-TAL MOF-i pürolüütiline metamorfoos kõrge jõudlusega lämmastikuga dopeeritud süsinikkatalüsaatoriks hapniku redutseerimisreaktsiooni jaoks

Lühikokkuvõte:

Metall-orgaanilised võrestikud (MOF-id) on paljulubavad lähteained suure jõudlusega metall-lämmastik-süsinik (M-N-C) elektrokatalüsaatorite sünteesiks. Siiski laguneb MOF-ide algne struktuurne terviklikkus pürolüüsi käigus sageli, mille tulemuseks on katalüütiliselt mitteaktiivsete metall-agregaatide moodustumine hapniku redutseerimisreaktsioonil (ORR). Käesolevas uuringus kirjeldatakse Zn-põhise MOF-i pürolüütilist muundumist Zn-N-C elektrokatalüsaatoriks. Katalüsaatori lähteaine Zn-TAL MOF optimeeritud pürolüüs võimaldas säilitada selle omase sfäärilise morfoloogia ning tsingi suhteliselt madal keemistemperatuur aitas vältida Zn-agregaatide teket. Pürolüüs temperatuuril 1000 °C andis tulemuseks tugevalt poorsete omadustega katalüsaatori ZnMOF-1000 (S_{BET} = 615 m^2 g^{-1}), millel oli suurepärane ORR-jõudlus: alguspotentsiaal (E_{onset}) 0,98 V ja poollainepotentsiaal ($E_{1/2}$) 0,84 V pöörduva vesinikelektroodi (RHE) suhtes, mis on võrreldav kommertsiaalse Pt/C katalüsaatoriga. Füüsikalised iseloomustamised (SEM, PXRD, XPS, MP-AES, gaasi füüsisorptsioon) viidi läbi materjali morfoloogia, tsingi agregaatide puudumise ja katalüsaatori koostise hindamiseks. Anioonvahetusmembraaniga kütuseelemendis (AEMFC) saavutas ZnMOF-1000 maksimaalse võimsustiheduse 553 mW cm^{-2} temperatuuril 60 °C. Tulemused näitavad, et Zn-TAL MOF on paljutõotav lähteaine Zn-N-C tüüpi katalüsaatorite sünteesiks, pakkudes tõhusat plaatinavaba alternatiivi kütuseelementide katoodkatalüsaatoritele.

Võtmesõnad: Hapniku redutseerimisreaktsioon (ORR), Elektrokeemia, Metall-orgaanilised võrestikud (MOF-id), Lämmastikuga dopeeritud süsinikkatalüsaator

CERCS: P395 Organometalliline keemia, P400 Füüsikaline keemia, P401 Elektrokeemia

TABLE OF CONTENTS

TERMS, ABBREVIATIONS AND NOTATIONS

AEM – Anion exchange membrane

AEMFC – Anion exchange membrane fuel cell

BET – Brunauer-Emmett-Teller

C_{dl} – Double-layer capacitance

CFEG – Cold field emission gun

C_s – Specific capacitance of the electrocatalyst

CV – Cyclic voltammetry

CVD – Chemical vapour deposition

EDX – Energy-dispersive X-ray spectrometer

EIS – Electrochemical Impedance Spectroscopy

E_{onset} – Onset potential

$E_{1/2}$ – Half-wave potential

ECSA – Electrochemical surface area

GC – Glassy carbon

HAADF-STEM – High annular dark-field scanning transmission electron microscopy

HDPE – High-density polyethylene

K-L – Koutecky-Levich

M-N-C – Metal-nitrogen-carbon

MOF – Metal-organic framework

n – The electron transfer number

NPC – Nitrogen-doped porous carbon

OCV – Open-circuit voltage

ORR – Oxygen reduction reaction

PEMFC – Proton exchange membrane fuel cells

PGM – Platinum group metal

PSD – Pore size distribution

PVD – Polyvinylpyrrolidone

PXRD – Powder X-ray diffraction

RDE – Rotating disc electrode

RHE – Reversible hydrogen electrode

S_{BET} – The Brunauer-Emmett-Teller surface area

SE – Secondary electron

S_{dft} – The surface area calculated using Density Functional Theory

SLPM – Standard litre per minute

SEM – Scanning electron microscopy

TGA – Thermogravimetric analysis

TD-DTA – Thermogravimetry-differential thermal analyzer

V_{μ} – Total volume of micropores

V_{tot} – The total pore volume

XPS – X-ray photoelectron spectroscopy

XRD – X-ray diffraction

ZIF-8 – Zeolitic imidazolate framework - 8

ZIF-67 – Zeolitic imidazolate framework - 67

QSDFT – Quenched solid density functional theory

INTRODUCTION

As the energy rate increases, fossil fuels are expected to stay the main energy source in the short term [1]. Yet, using fossil fuels for energy releases high levels of CO_2, causing environmental issues, climate change, and health concerns [1]. Fuel cells are being researched as they offer high energy density, are cost-effective, and are environmentally friendly, using hydrogen for energy storage from green but intermittent renewable energy sources [2]. These next-generation energy conversion devices can help solve problems associated with fossil fuel depletion and its environmental impact.

The electrochemical oxygen reduction reaction (ORR) at the cathode is a major problem hindering the commercial use of fuel cells. Improving the efficiency of ORR for large-scale implementation of fuel cells is possible with the right catalyst, which will allow the ORR to occur at lower overpotentials. Although platinum group metals-based (PGMs) catalysts are currently the best due to electrochemical efficiency [3], their limited supply, high cost, and stability issues make the development of alternative base metal catalysts a high priority [4,5]. Therefore, transition metal nitrogen-doped carbon catalysts M–N–C are an attractive alternative for fuel cells due to their lower cost and sufficient ORR performance [6]. Metal-organic frameworks (MOFs) are promising precursors for ORR catalysts. Their structure, tunable properties, high porosity and large surface area make MOF-based carbon electrocatalysts efficient for ORR. The uniform distribution of metal atoms in MOF provides a more homogeneous and efficient M-N-C catalyst after pyrolysis [7]. Zn-MOF-derived M–N–C catalysts have demonstrated good activity and stability, making them an interesting candidate for ORR electrocatalyst research and development [8].

In this study, we investigate new M-N-C catalysts for ORR using Zn-based metal-organic hollow spheres as a precursor - Zn-TAL MOF. The precursor was prepared by reacting zinc chloride with 1H-Benzo[d]imidazole-5,6-diol, which was selected as a carbon/nitrogen-rich ligand. Next, Zn-TAL MOF was pyrolysed at different temperatures (700 ℃, 800 ℃, 900 ℃, and 1000 ℃) to find the optimal temperature for the synthesis of Zn-N-C, the catalyst with the best electrocatalytic activity. To establish structural and compositional properties, the morphological studies of the produced catalysts ZnMOF-700, ZnMOF-800, ZnMOF-900, and ZnMOF-1000 were performed. Electrochemical activity towards ORR was tested and correlated with the catalyst morphology and composition.

1. LITERATURE REVIEW

1.1 Fuel cells

Fuel cells offer significant promise for the transition to a sustainable energy future by providing clean, efficient, and reliable power generation solutions for many diverse applications [9]. A fuel cell is an electrochemical device that generates electricity directly from the chemical reaction between a fuel and an oxidant. In a typical fuel cell (Figure 1), hydrogen is fed into the anode (negative electrode) (Figure 1a), and oxygen is fed into the cathode (positive electrode) (Figure 1b). At the anode, hydrogen molecules dissociate into protons and electrons. The protons move through an electrolyte to the cathode, while the electrons generate an electrical current, flowing through an external circuit (Figure 1c). At the cathode (Figure 1b), the oxygen, protons and electrons combine to produce water as the main byproduct [9].

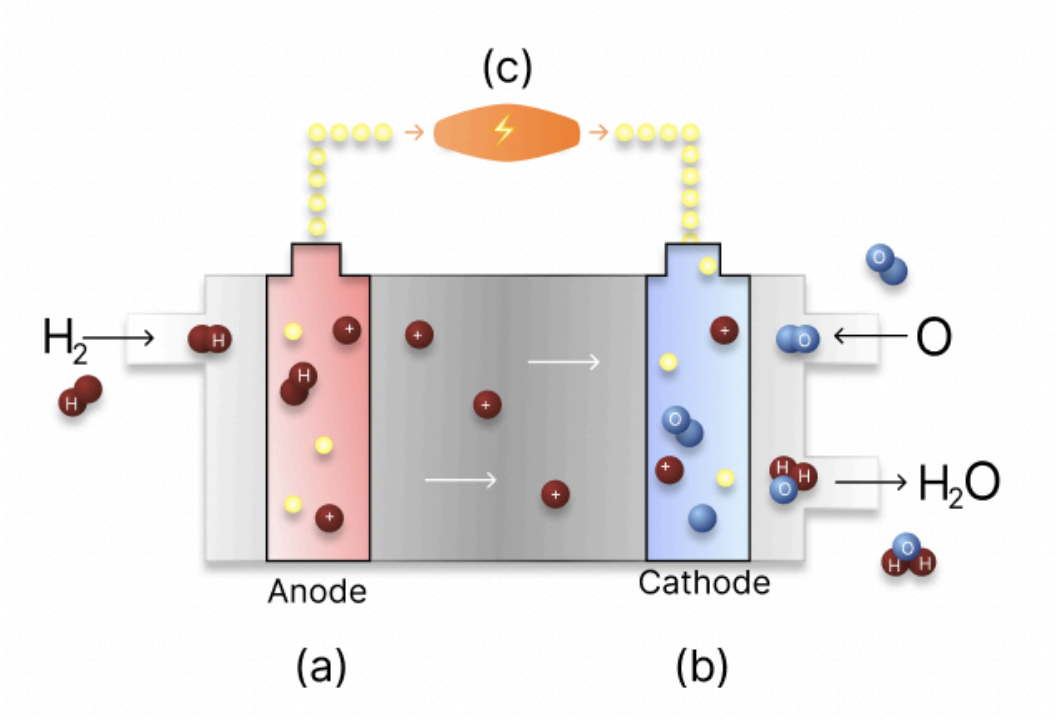

Figure 1. Schematic depiction of a fuel cell: (a) anode, where hydrogen molecules dissociate into protons and electrons; (b) cathode, where the protons, electrons, and oxygen combine to produce water as the main byproduct; (c) electrical current.

Fuel cells have gained widespread attention due to their numerous advantages, including high power density, affordability (the cost is projected to be $179 per kWnet when manufactured at a volume of 50,000 units per year [10], and environmental friendliness.

Power density measures the rate at which energy can be discharged from the fuel cell system. Typically expressed in units of W per kg or W per litre, higher power density indicates the ability to deliver power to larger loads efficiently [11]. The latest mass-producible fuel cell stacks demonstrate a system power over 100 kW, and power density greater than 3.1 kW L^{-1} while lasting for 5,000 to 20,000 hours [12]. Fuel cells allow for harnessing the potential of hydrogen as a clean and sustainable energy source. Hydrogen possesses a high energy density (39.4 kWh kg^{-1}), and the production of green hydrogen is rapidly advancing, reaching industrial levels (Figure 2) [13]. The world's production of hydrogen is projected to nearly double, associated with the world's shift towards cleaner energy sources and efforts to decarbonize various sectors, including transport and industry. Technological progress and government support are also accelerating this growth.

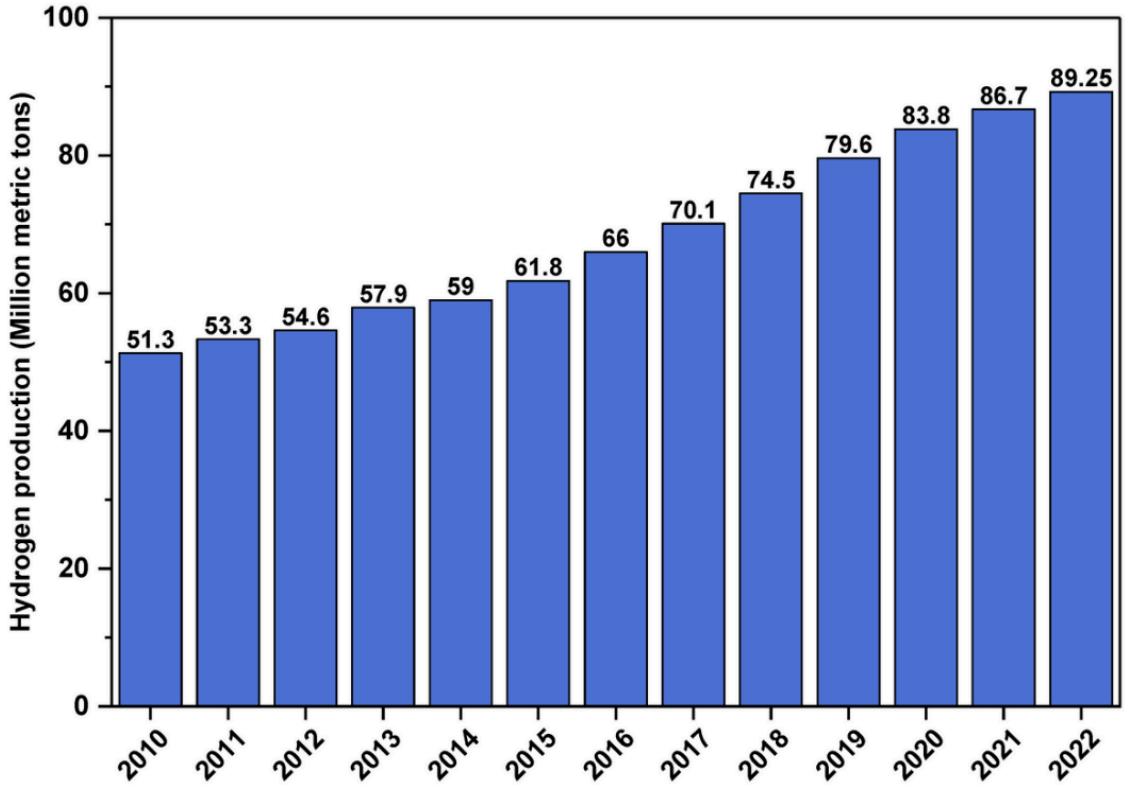

Figure 2. Analysis of global hydrogen production trends, 2010-2022 [14].

Furthermore, fuel cells are good for the environment because they produce electricity through an electrochemical process that emits only water and heat as byproducts, unlike traditional power generation methods that often release harmful pollutants and greenhouse gases [15].

1.2 The chemistry behind hydrogen fuel cells

In order to further improve the fuel cell system, it is important to know the reactions occurring inside. The electrochemical reactions that occur within the fuel cell drive the hydrogen fuel cell's chemical process. These reactions follow the principles of redox (reduction-oxidation) reactions and involve the movement of charged particles, protons, and electrons [16].

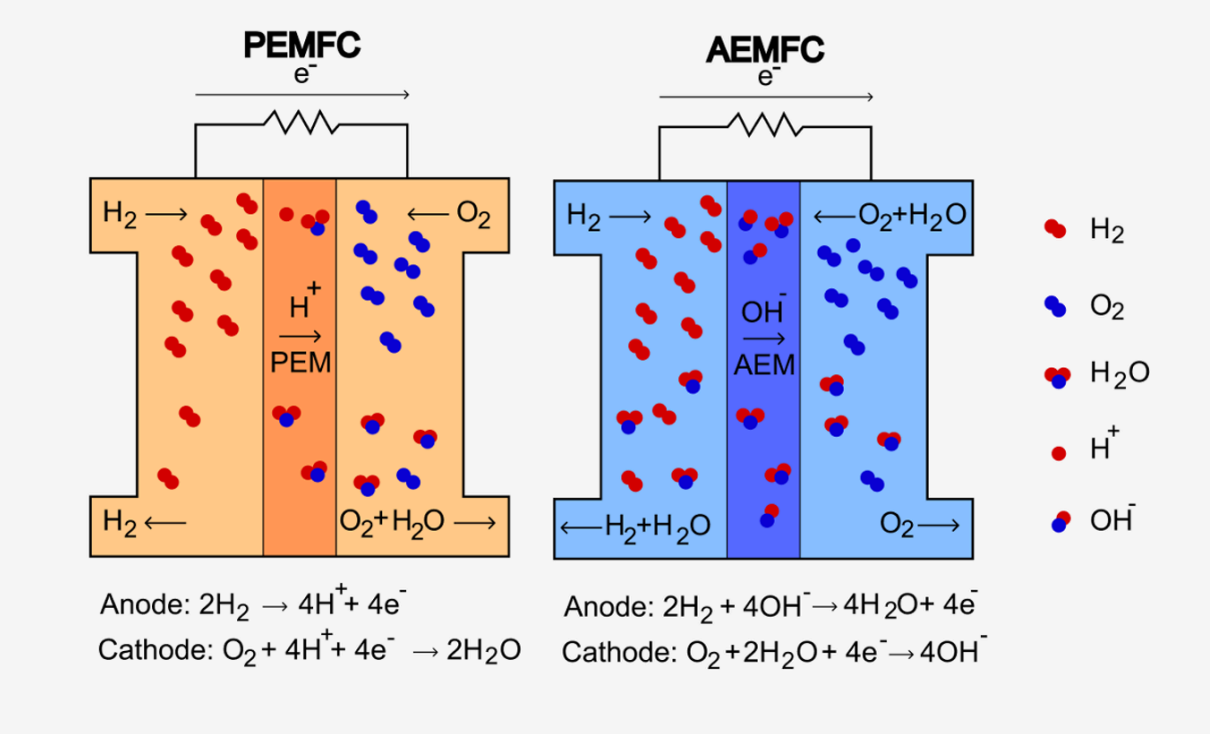

Figure 3. Schematic diagrams of (a) a PEMFC and (b) an AEMFC, with the relevant electrode reactions [17].

1.2.1 Acidic conditions

Operation in acidic conditions is characteristic of a Proton Exchange Membrane Fuel Cell (PEMFC) (Figure 3a). The acidic environment facilitates proton conduction from anode to cathode via the proton-conducting electrolyte or membrane. In PEMFC, first, the hydrogen (H_2) is supplied to the anode, where a hydrogen oxidation reaction (HOR) takes place (Equation 1). At the anode, the hydrogen molecules dissociate into protons (H^+) and electrons (e^-) on a catalyst surface [18]:

$$H_2 \rightarrow 2H^+ + 2e^- \quad (1)$$

Protons move through the electrolyte, and electrons go through a circuit, generating electricity. Then, on the cathode, oxygen (O_2) undergoes an Oxygen Reduction Reaction (ORR) and combines with electrons (e^-) and protons (H^+) to produce water (Equation 2) [18].

Via a more preferred direct $4e^-$ pathway:

$$O_2 + 4H^+ + 4e^- \rightarrow 2H_2O \qquad E^0 = 1.230\ V \qquad (2)$$

Or less-desired $2e^-$ pathway:

$$O_2 + 2H^+ + 2e^- \rightarrow H_2O_2 \qquad E^0 = 0.695\ V \qquad (3)$$

$$H_2O_2 + 2H^+ + 2e^- \rightarrow 2H_2O \qquad E^0 = 1.230\ V \qquad (4)$$

The overall reaction in a hydrogen fuel cell in acidic conditions can be represented as:

$$2H_2 + O_2 \rightarrow 2H_2O \qquad (5)$$

This reaction confirms that the fuel cell system's only byproduct is water, making it a clean and environmentally friendly energy conversion technology [19].

1.2.2 Alkaline conditions

In Anion Exchange Membrane Fuel Cells (AEMFCs), alkaline conditions are provided by the alkaline electrolyte, typically a solution of potassium hydroxide (KOH) (Figure 3b) [20]. Unlike PEMFCs, which use acidic membranes to transfer protons, AEMFCs use alkaline exchange membranes to conduct hydroxide ions (OH^-). The KOH solution provides the high concentration of hydroxide ions necessary for the electrochemical reactions to proceed efficiently. The hydroxide ions are crucial for the ORR at the cathode, where they participate directly in the reaction.

In alkaline media, the ORR preferably proceeds via a 4-electron pathway (Equation 6).

$$O_2 + 2H_2O + 4e^- \rightarrow 4OH^- \qquad E^0 = 1.230\ V \qquad (6)$$

Similar to acidic media, a less desirable 2-electron pathway can also occur. This pathway involves the direct addition of two electrons to oxygen, forming a superoxide anion (HO_2^-). This is often a significant side reaction competing with the desired four-electron pathway.

$$O_2 + H_2O + 2e^- \rightarrow HO_2^- + OH^- \qquad E^0 = 0.695\ V \qquad (7)$$

$$HO_2^- + 2e^- + 2H_2O \rightarrow 3OH^- \qquad E^0 = 1.230\ V \qquad (8)$$

Optimising the ORR efficiency to favour the direct four-electron pathway requires tuning the adsorption energies of reaction intermediates. This is practically achieved by modifying the

active site's composition (e.g., metal centre, coordination species, N-species) and enhancing both the active site density and accessibility. Increasing fuel cell efficiency while preserving its eco-friendliness requires improving the ORR — a key, rate-limiting step in fuel cell operations.

Overall, the ORR mechanism involves a series of steps, including oxygen adsorption, activation, proton transfer, electron transfer, and the formation of water molecules (Figure 4). So, the possible pathway for processing O_2 is to break the O-O bond in O_2 at the adsorption site to create O species, which are then reduced to OH and further to H_2O [20,21].

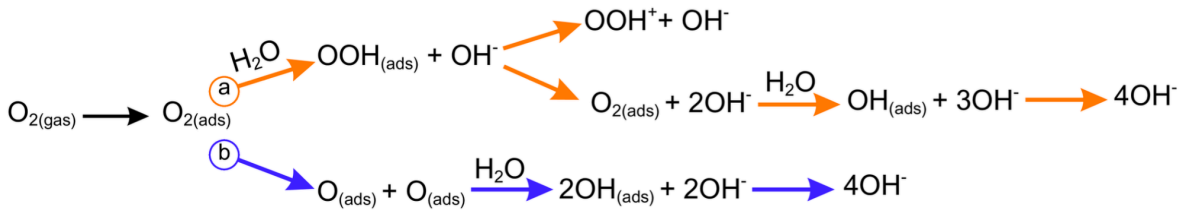

Figure 4. The reaction scheme of ORR in an alkaline solution is (a) an associative pathway and (b) a dissociative pathway.

The oxygen reduction reaction (ORR) proceeds via multiple pathways influenced by pH and catalyst properties. Two proposed mechanisms are associative and dissociative. The dissociative pathway involves O_2 adsorption across two metal sites, breaking the O-O bond and bypassing peroxide intermediates. However, this pathway is generally less favourable due to the high energy required to cleave the O-O bond. Conversely, the associative pathway involves O_2 adsorption on a single site, facilitating O-O bond breakage and the formation of peroxide intermediates [22]. The efficiency and kinetics of these steps are influenced by factors such as catalyst activity, which are key determinants of the ORR performance in fuel cells. In particular, the catalyst determines if the reaction follows the $4e^-$ or the $2e^-$ ORR [23], defining the ORR selectivity towards H_2O or H_2O_2. Furthermore, considering the different bonding modes of the oxygen intermediates, a catalyst with optimised adsorption energies is required to achieve the best performance.

1.3 Catalysts for ORR

In the ORR process, a catalyst plays a crucial role in facilitating and accelerating the reaction kinetics [24]. The catalyst is a material that can increase the rate of the ORR by providing

active sites for oxygen adsorption, activation, and electron transfer. Today, platinum group metals (PGMs) remain the benchmark for application in ORR due to their activity and stability [25]. However, the expensiveness and scarcity of PGMs [26] directed research efforts to find alternative catalyst materials. Among recently developed catalysts, single-atom site catalysts stand out as a viable option to replace PGMs. In particular, transition metal nitrogen-doped carbon catalysts (M-N-C) show potential as a good alternative due to the abundance of active sites for catalysing the ORR [25,27], and their improved stability [28]. More specifically, M-N-C catalysts feature various nitrogen species resulting from nitrogen doping into carbon structures. They are mainly categorised into four types: pyridinic, graphitic, pyrrolic, and oxidised nitrogen [29], which often co-exist, and the ratio of each is usually random. Although it is still debated which type of N-species is the major contributor to the ORR activity, their ORR promotion effect is evidenced by previous studies [30].

Nevertheless, in M-N-Cs, the main focus is on the single-atom sites with the MN_4 structure, which exhibit extraordinary catalytic activity for ORR. In MN_4, the transition metal centre is tetracoordinated to nitrogen atoms, all situated in an extended carbon-based matrix. In the MN_4, nitrogens become an electron-withdrawing ligand [31], effectively regulating the electronic structure of transition metal and optimising the adsorption between metal and oxygen species [32]. Additionally, the presence of transition metals facilitates electron transfer processes, promoting faster reaction kinetics and enhanced performance in ORR. There are many different ways to obtain M-N-C [33], but there is one that attracts a lot of attention in chemistry at the moment - using metal-organic frameworks as M-N-C precursors [34].

1.4. MOFs-derived catalysts in ORR

MOFs are a class of materials consisting of metal ions bound to organic ligands, and their unique structure and tunable properties make them a potential candidate as catalysts for ORR applications. Due to their structural flexibility, high porosity, and large surface area, carbon-based electrocatalysts derived from MOFs have generated considerable interest as effective catalysts for ORR [35].

In the context of ORR, MOF-based catalysts have demonstrated enhanced activity, selectivity, and stability, making them attractive for applications in fuel cells. MOFs evenly distribute metal atoms, creating a more uniform metal atom distribution after pyrolysis and, thus, a more efficient M-N-C catalyst [36].

Numerous studies have explored MOF-templated nitrogen-doped porous carbons (NPCs), varying MOF templates, temperatures, precursors, pyrolysis methods, and post-synthetic functionalisation to leverage MOFs' high surface area and tunable porosity [37].

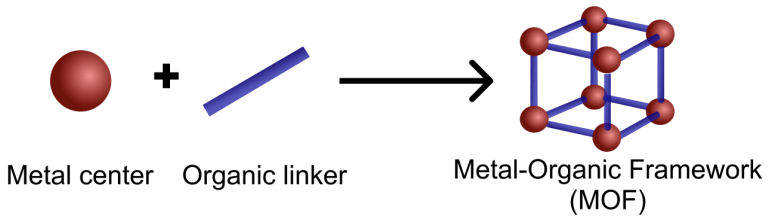

Figure 5. Schematic depiction of MOF materials.

Ligands play a crucial role in coordination chemistry by stabilising and defining the coordination geometry around the metal atom, influencing the complex's stability and reactivity. Ligands donate electron pairs to the metal atom, creating coordinate covalent bonds. This interaction determines the structure and properties of the complex [38,39]. MOFs have shown promise as catalysts for various reactions, including organic transformations and green chemistry processes [40].

There are numerous previous on the metal-organic framework for the synthesis of M-N-C catalysts. Specifically, Jing et al. found that adding a nickel catalyst to CoFe nanoporous carbon enhanced ORR activity and long-term stability [41]. To create stable, highly graphitized porous carbon, their study uses a three-step (corrosion, pyrolysis, and replacement) method to synthesize N-enriched hollow carbon (CoFeNi/NC) from PVP/ZIF-8/ZIF-67. The synthesised CoFeNi/NC exhibited excellent ORR performance (current density 2.593 mA cm^{-2}, onset potential of 0.914 V vs. RHE) due to its high graphitisation, hollow structure, and CoFeNi co-doping. Maintaining 95.4% of its initial performance after 12 hours, CoFeNi/NC shows promise as an efficient electrocatalyst [42]. Another study done by Huang used ZIF-8 MOF as support for chemical vapour deposition (CVD), which allows efficient metal distribution on the materials during pyrolysis. Iron salt vapours deposited on ZIF-8 replace Zn with Fe, forming a Fe-N-C catalyst with uniformly distributed Fe-N_4 centres [43]. Additionally, in 2021, Yang et al. synthesised the Mn/C-NO catalyst by pyrolysis of Mn-1,3,5-benzenetricarboxylic acid framework (Mn-BTC MOF) in nitrogen, followed by acid etching and calculation in ammonia, which led to the formation of Mn/C-NO with single NO bonds. In their study, high-angle annular dark-field scanning transmission electron microscopy HAADF-STEM and X-ray absorption spectroscopy XAS confirmed the successful formation of single Mn atom sites coordinated to O and N. Their

catalyst showed good activity in alkaline electrolyte (E_{onset} = 0.93 V, $E_{1/2}$ = 0.80 V vs. RHE) [44]. Thus, the previous results prove that MOFs are a versatile platform for further investigation to achieve optimal ORR performance, serving as a foundation for the current study.

In this work, we present a Zn-based MOF developed from a carbon/nitrogen-rich 1H-benzo[d]imidazole-5,6-diol ligand and Zn metal nodes, used here as a single precursor to produce a highly efficient oxygen reduction electrocatalyst. The synthesised Zn-TAL was pyrolysed at four different temperatures (700, 800, 900, and 1000 °C) to find the optimal pyrolysis conditions, which allows for retaining the hollow sphere structure and inhibits the formation of Zn-aggregates. The produced Zn-N-C samples - ZnMOF-700, ZnMOF-800, ZnMOF-900 and ZnMOF-1000 were characterised with spectroscopic methods to establish and assess their structural and compositional differences. The produced samples were thoroughly tested for their ORR electrochemical performance, and their activity was related to their structural properties.

2. THE AIMS OF THE THESIS

Aim #1. To synthesize efficient Zn-TAL metal-organic-framework derived Zn-N-C catalysts.

Aim #2. To characterise catalyst materials using multiple physical characterisation methods.

Aim #3. To conduct electrochemical experiments and determine the main ORR kinetic parameters for synthesized catalysts toward ORR.

Aim #4. To test the most promising catalyst in AEMFC configuration.

Aim #5. To investigate the link between structural characteristics, composition and ORR activity.

3. EXPERIMENTAL PART

3.1. MATERIALS AND METHODS

3.1.1. Chemicals and materials

Aqueous ammonium hydroxide solution (25%, Lach-ner), Zinc chloride ($ZnCl_2$, ≥ 98%, Honeywell), N,N-Dimethylformamide (C_3H_7NO, ≥ 99,8%, Sigma-Aldrich) were used as received. All solutions were prepared using Ultrapure water (18.2 MΩ cm; Milli-Q purification system by Millipore). A tubular furnace (Carbolite Gero EST 12/300B) was utilised for the post-synthetic pyrolysis of electrocatalysts.

3.1.2. Synthesis

Synthesis of 1H-Benzo[d]imidazole-5,6-diol

1H-benzo[d]imidazole-5,6-diol ($C_7H_6N_2O_2$) was synthesised in four steps as described in the published procedure [44]. 5,6-Dimethoxy-1H-benzo[d]imidazole (7.79 g, 43.7 mmol, 1.0 equiv) was added into HBr (48%, 50 mL), and stirred at 120 ℃. After 4 h, the reaction was cooled down to 0 ℃, and solids were collected and washed with petroleum ether to give the desired product as a colourless powder (4.59 g, 30.6 mmol, 70%). 1 H NMR (400 MHz, DMSO) δ 9.75 (s, 2H), 9.25 (s, 1H), 7.12 (s, 2H). 13C NMR (100 MHz, DMSO) δ 146.4, 136.9, 123.7, 98.4.

Synthesis of Zn-TAL:

Zn-TAL metal-organic hollow spheres were synthesised by dropping $ZnCl_2$ (1.38 g, 10.1 mmol, 0.5 equiv) into a mixture of 1H-benzo[d]imidazole-5,6-diol (3.0 g, 20. 2 mmol, 2.0 equiv) in 25% aq.NH_3/DMF/EtOH/water. The resulting solution was stirred at room temperature for 24 h. Afterwards, the precipitate was isolated via filtration, washed with ethanol and dried for 12 hours at 60 °C. Zn-TAL final mass was 0.83 g.

Prepared Zn-TAL underwent a 1 h pyrolysis at various temperatures in an N_2 atmosphere (700, 800, 900, and 1000 ℃, temperature ramping 20 degrees per minute) and subsequent acid etching with 3 M HCl for 12 h at room temperature. Acid-etched samples were filtered, washed with deionised water, dried and pyrolysed. The resulting materials were designated as ZnMOF-700, ZnMOF-800, ZnMOF-900 and ZnMOF-1000.

3.1.3. Physical Characterisation

Thermogravimetric analysis (TGA)

The thermogravimetric analysis - differential thermal analysis (TG-DTA) experiments were conducted by Dr. Tiit Kaljuvee (TalTech) using a Setaram Labsys Evo 1600 thermal analyser, performed in an Ar atmosphere as follows: the Zn-TAL MOF was heated to 1000 °C at a heating rate of 10 °C min^{-1} under non-isothermal conditions Afterwards, the material was cooled to 30 °C at a heating rate of 50 °C min^{-1} under non-isothermal conditions. Standard alumina crucibles with a volume of 100 μL were utilised with a sample mass of 50 mg, and the gas flow rate was set at 20 mL min^{-1}.

Nitrogen physisorption measurements

The porosity parameters of the prepared catalysts were assessed by low-temperature N_2 adsorption with a NOVAtouch LX2 (Quantachrome Instruments). Before measurement, the catalysts were degassed in a vacuum at 200 °C for 16 hours. The BET surface area (S_{BET}) of the materials was calculated with a P/P_0 interval of 0.02 - 0.2. The total pore volume (V_{tot}) was calculated with a value of P/P_0 of 0.97. Pore size distribution (PSD) and specific surface area (S_{dft}) were derived from N_2 isotherms employing a quenched solid density functional theory (QSDFT) equilibrium model designed for slit-type pores. (Gas physisorption measurements and data analysis were provided by Dr. Maike Käärik and Prof. Jaan Leis, University of Tartu).

Powder X-ray Diffraction (PXRD) analysis

The PXRD analysis was performed by Dr. Jaan Aruväli (University of Tartu) using Bruker D8 Advance diffractometer with Ni-filtered Cu Kα as a radiation source and LynxEye line detector. The powder samples were measured in a range of 3° to 93° 2θ using a scanning step of 0.013° 2θ and a counting time of 356 s per step (PXRD analysis was performed by Dr. Jaan Aruväli from the Institute of Ecology and Earth Sciences Department of Geology, (University of Tartu).

X-ray Photoelectron Spectroscopy (XPS)

Ultra-high vacuum conditions were used for conducting XPS using a non-monochromatic twin anode X-ray tube (Thermo XR3E2) with the characteristic energy of 1,253.6 eV (Mg

Kα) and an electron energy analyser SCIENTA SES 100. Catalyst suspensions in isopropanol with a concentration of 4 mg mL^{-1} were deposited onto GC plates (1.1×1.1 cm) for sample preparation. The survey scan was collected using the energy range from 900 to 0 eV, pass energy of 200 eV, step size of 0.5 eV, step duration of 0.2 s, and a scan number of 5. High-resolution XPS scans were performed using pass energy 200 eV and step size 0.1 eV. An Ag wire attached to the sample holders was used for energy reference (Ag 3d5/2 at 367.8 eV); no charging effects were observed. Peak fitting was done using CasaXPS (version 2.3.16) software. The Gauss–Lorentz hybrid function (GL 70, Gauss 30%, Lorentz 70%) and a blend of linear and Shirley-type backgrounds were used for peak fitting. (Measurements and peak analysis provided by Dr. Arvo Kikas and Prof. Vambola Kisand from the Institute of Physics, University of Tartu)

Scanning Electron Microscopy and Energy-Dispersive X-ray Spectroscopy (SEM EDX)

The morphology of ZnMOF samples was investigated by SEM with CFEG made by Hitachi High Technologies (Japan) model S5500, equipped with energy-dispersive x-ray spectrometer Thermo Fisher Noran System Six. The imaging was carried out at an accelerating voltage of 30 keV in secondary electron and bright field transmission (BF-STEM) mode at a magnification range of 10-200k times. The EDX analyses were performed at 5 keV and 30 keV. The lower energy was used to better characterise low energy peaks in the range of C, N, and Zn. (SEM images for non-pyrolysed provided by Sven Oras (Institute of Physics, University of Tartu), Lukaz pyrolised (Warsaw University of Technology).

Microwave Plasma-Atomic Emission Spectroscopy (MP-AES)

MP-AES was utilised to analyse the bulk metal composition in the catalyst samples. The analysis was conducted using Agilent 4210 MP-AES. Microwave digestion system (Anton Paar Multiwave PRO) was utilised to prepare samples by dissolving the catalysts (10 mg each) in a mixture of 2 mL of H_2O_2 and 4 mL of HNO_3 in NXF100 vessels (PTFE/TFM liner). Digestion conditions: at 230 °C, pressures in the range of 45 and 50 bar. Afterwards, the metal concentration was diluted to 5 mg L^{-1} with 2% HNO_3. Elemental analysis was conducted using the PerkinElmer@2400 Series II CHNSO/O Elemental Analyzer. (MP-AES experiments done by Dr. Peeter Paaver from the Institute of Ecology and Earth Sciences Department of Geology, University of Tartu)

3.1.4. Electrochemical characterisation

Electrochemical measurements were conducted using a standard three-electrode configuration, with a glassy carbon (GC) disk electrode as the working electrode, a reversible hydrogen electrode (RHE) as the reference electrode, and a GC rod as the counter electrode. Autolab PGSTAT128N potentiostat/galvanostat controlled by Nova 2.1.7 software was used to apply the potential. A GC rotating disc electrode (RDE) was regulated by the OrigaBox speed controller unit and rotated at various speeds (ω = 400, 620, 900, 1225, 1600, and 2025 rpm). Fresh alkaline electrolyte solutions were prepared with KOH pellets (99.99%, Sigma-Aldrich) and Milli-Q water. Electrolytes were saturated with pure O_2 (99.999%, Linde Gas) for ORR experiments and with Ar (99.999%, Linde Gas) to eliminate oxygen for recording the cyclic voltammetry (CV) curves. The GC electrodes (diameter: 5 mm) were polished with 1 and 0.3 μm alumina slurries and sonicated in both isopropanol and Milli-Q water for 3 min to eliminate any remaining abrasive particles. 5 mg of electrocatalyst powder was dispersed in 200 μL of a 0.5% Nafion solution (Sigma-Aldrich) in 2-propanol and sonicated for 5 min to prepare a uniform ink. Then, 4 μL of the resulting electrocatalyst suspension was drop-cast onto a GC electrode with a mass loading of 0.5 mg cm^{-2} and dried in ambient air at room temperature. The commercial 20 wt% Pt/C (E-TEK) was employed as a benchmark for ORR using the same protocol for preparing ink and working electrodes. Selected electrocatalysts underwent accelerated stability testing according to a protocol of 5000 potential cycles from +1.0 to +0.6 V vs. RHE, with a scan rate of 50 mV s^{-1}, at a rotation rate of 1600 rpm in an O_2-saturated electrolyte.

3.1.5. Anion exchange membrane fuel cell testing

In order to illustrate the practical application in an anion exchange membrane fuel cell (AEMFC), the ZnMOF-1000 electrocatalyst was prepared as a cathode following previously reported procedures [45,46]. The cathode and anode were loaded to 1 $mg_{ZnMOF\text{-}1000}$ cm^{-2} and 0.6 mg_{PtRu} cm^{-2}, respectively, while a high-density polyethylene (HDPE) based AEM was utilized. The AEMFC was examined in a Scribner Associates 850E test station operated at a cell temperature of 60 °C, with an anode humidifier temperature set at 54 °C and a cathode humidifier temperature at 56 °C. The gas flow rates for both hydrogen and oxygen were maintained at 1 standard litre per minute (SLPM), with a back-pressure of 100 kPag. The polarisation curve was obtained by scanning from the open-circuit voltage (OCV) of ~1 V to

0.1 V at a scan rate of 10 mV sec^{-1}. (AEMFC was performed by Dr. John Douglin, Prof. Dario Dekel, from Technion Israel Institute of Technology).

4. RESULTS AND DISCUSSION

4.1. Synthesis

After dissolving the ligand, zinc chloride was added dropwise (Figure 6a), resulting in the colour change from colourless to dark green, indicating the reaction between components. More specifically, the ligand is coordinated with zinc nodes to form Zn-TAL metal-organic hollow spheres with an approximated structural unit depicted in (Figure 6b).

After that, Zn-TAL was pyrolysed, yielding Zn-N-C hollow spheres (Figure 6c). The right choice of a ligand is of great importance for catalyst precursors because the ligand can significantly affect the catalytic activity, selectivity, and stability of the catalyst [47]. The ligand used in this synthesis (1H-benzo[d]imidazole-5,6-diol) was selected as a carbon/nitrogen-rich polydentate ligand equipped with effective coordination groups to boost multidirectional ligating properties. Furthermore, after pyrolysis, 1H-benzo[d]imidazole-5,6-diol-derived catalyst materials demonstrate high porosity, surface area and catalytic activity due to the formation of unique asymmetric scaffolds [48].

When choosing a metal for a catalyst, attention was paid to the advantage in terms of the efficiency of the final catalyst. First, the Zn-derived M-N-C have shown good activity and stability [49]. Additionally, a very intriguing characteristic of Zn-based metal-organic precursors is the evaporation of Zn metal at ca. 625 ℃. In this study, evaporation of Zn played a key role in the formation of ZnN_4 single-atom sites. More specifically, during pyrolysis, non-coordinated Zn atoms tend to agglomerate, which result in the decrease of surface area and catalytic graphitisation [50]. Therefore, pyrolysis at elevated temperatures allowed us to evaporate the less stable Zn-agglomerates, retaining ZnN_4 single-atom sites. Additionally, by avoiding graphitisation, we retain the porous carbon hollow sphere frame [51].

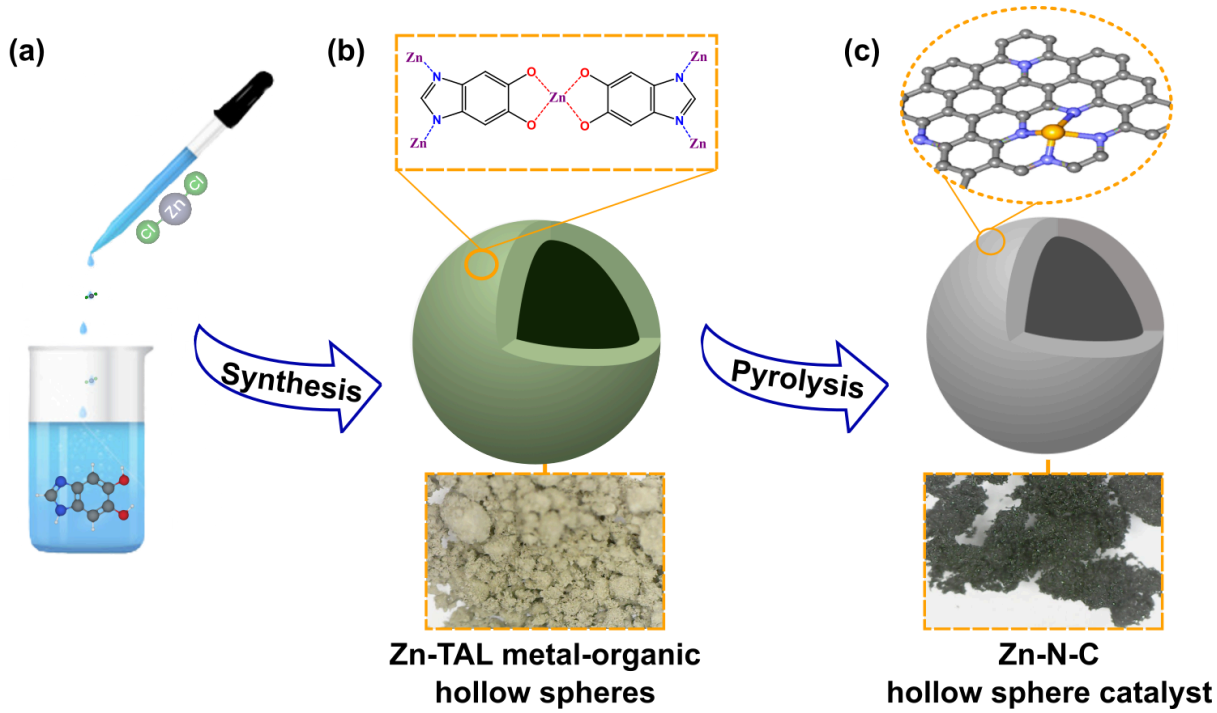

Figure 6. Synthesis scheme for Zn-N-C catalysts (a) preparation of Zn-TAL. (b) model of a Zn-TAL hollow sphere. (c) model of pyrolysed Zn-TAL hollow sphere.

In this study, heat treatment at temperatures of 700, 800, 900, and 1000 °C was applied to find out how pyrolysis affects the structural properties and catalytic activity of ZnMOF. Thus, at first, to understand the behaviour of Zn-TAL during pyrolysis, TGA was performed, imitating the pyrolysis conditions. In TGA, the initial weight loss was observed in the range of 0-160 ℃, which was attributed to the evaporation of water and residual solvents in the structure. As the temperature keeps increasing, the weight loss is further observed in the range of 160-600 ℃, indicating the decomposition of organic matter in the synthesised Zn-TAL. At approximately 650 ℃, thermal weight loss was attributed to the evaporation of the clustered Zn particles, as discussed previously [52]. The thermal weight loss continues till 1000 ℃, suggesting that if there is any remaining Zn, it is in a more stable N_4-coordinated state, which enables Zn atoms to resist elevated temperatures without complete evaporation.

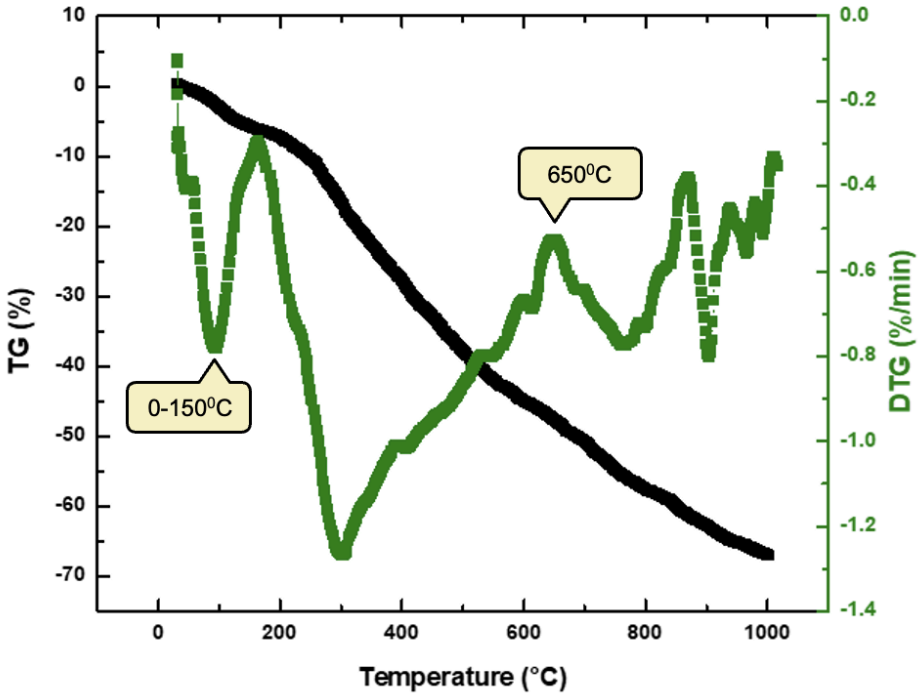

Figure 7. TGA curves obtained during pyrolysis of Zn-TAL.

4.2. Characterisation

4.2.1. Scanning electron microscopy

Through SEM, it has been determined that Zn-TAL has a structure consisting of fused hollow spheres. The particle size distribution (PSD) is crucial in understanding the properties of material, as it displays a trend of decreasing hollow spheres with rising temperatures. Raw Zn-TAL features the largest hollow spheres, with an average size of 140-160 nm, as shown in the graph. Following temperature increases, the hollow spheres in Zn-MOF-700 shrink slightly, ranging from 100-120 nm. Upon further heating, the hollow spheres continue to decrease in size, eventually measuring between 60-100 nm. While high temperatures are employed, the carbon framework of the material remains consistent, as only the hollow spheres change in size.

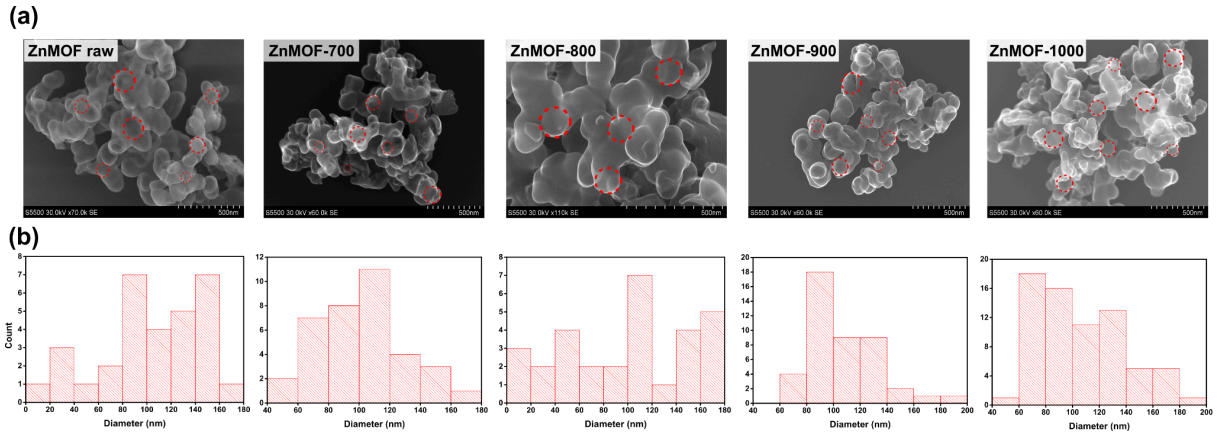

Figure 8. (a) SEM images of Zn-TAL (non-pyrolysed, pyrolysed at 700, 800, 900, 1000 ℃). (b) PSD graphs obtained for all prepared samples.

4.2.2. X-ray diffraction

Next, X-ray diffraction was used to identify the crystal structure of the catalysts. In the XRD, each peak corresponds to a specific set of planes in the crystal lattice, and the position and intensity of the peaks can be used to identify the crystalline phase. We were able to see that all 4 samples were structurally pure carbons without additional peaks indicating Zn compounds. With increasing pyrolysis temperature, the intensity of the (100) peak noticeably increases, which suggests that the crystalline structure of the material is becoming more ordered at higher temperatures. (Figure 9a).

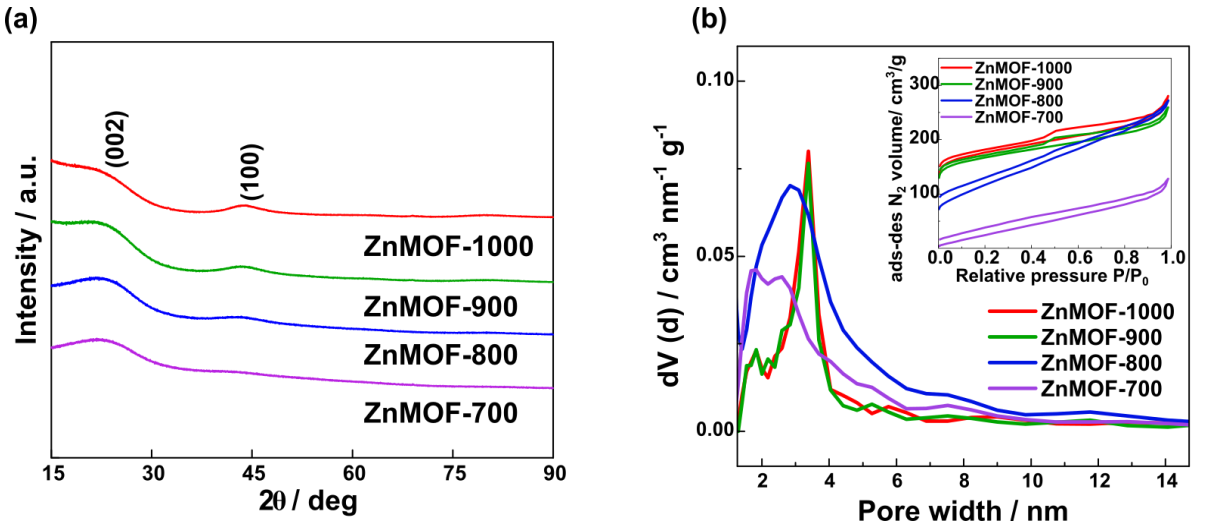

Figure 9. (a) X-ray diffraction patterns of ZnMOF catalysts; (b) pore size distribution and adsorption isotherms obtained for ZnMOF-700, ZnMOF-800, ZnMOF-900, and ZnMOF-1000.

4.2.3. Nitrogen physisorption

In order to understand the textural properties of pyrolysed samples after acid etching, N_2 physisorption was applied. If we look at the behaviour of ZnMOF-800, ZnMOF-900, ZnMOF-1000 samples at low relative pressure with increasing pyrolysis temperature, the isotherms increased at a high rate (Figure 9b), and all samples showed typical type IV isotherms with H4 type hysteresis loops in relative pressure range P/P0>0.4. The increase in the isotherms at low relative pressure with increasing pyrolysis temperature suggests that the samples are becoming more porous or that the pore size distribution is shifting towards larger pores, but still pore width graph shows intensive peaks from 1 to 4 which means that ZnMOF is a micro/mesoporous material. The BET surface areas of the ZnMOF catalysts ZnMOF-700, ZnMOF-800, ZnMOF-900, and ZnMOF-1000 are 103, 414, 584, and 615 g m^{-2}, respectively (Table 1). This suggests that ZnMOF-1000 has higher surface area which means it may have a higher number of active sites available for catalysis than the sample with the lower surface area.

Table 1. Textural properties of ZnMOF-700, ZnMOF-800, ZnMOF-900, and ZnMOF-1000.

Electrocatalyst	S_{BET} ($m^2 g^{-1}$)	S_{DFT} ($m^2 g^{-1}$)	V_{tot} ($cm^3 g^{-1}$)	V_{μ} ($cm^3 g^{-1}$)
ZnMOF-700	103	100	0.17	0.03
ZnMOF-800	414	475	0.40	0.14
ZnMOF-900	584	715	0.37	0.23
ZnMOF-1000	615	746	0.40	0.24

4.2.4. X-ray photoelectron spectroscopy

Through an X-ray photoelectron spectroscopy, the surface elemental composition of the prepared catalysts was analysed. The XPS survey spectra (Figure 10a), confirmed the presence of C, N, O, and Zn elements in all the catalysts under investigation, evidencing that

Zn is not completely evaporated. The high-resolution XPS C 1s spectra (Figure 10), revealed a range of carbon-containing species that were identified across the materials, such as C-C (283.5 eV), C-O (285.8 eV), C=O (290 eV, 288 eV), C=C (283.7 eV), C-C/C=C, carbide (282.6 eV) and pi-pi* (291.5eV) [53].

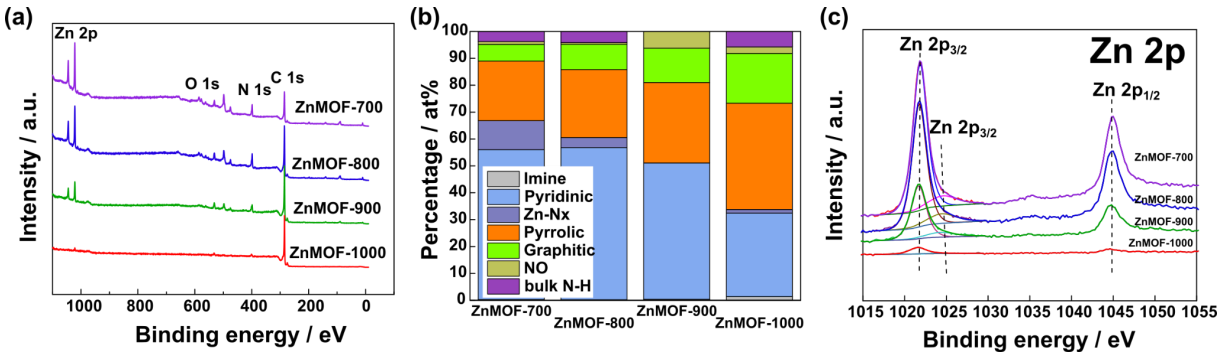

Figure 10. (a) The XPS survey spectra obtained for ZnMOF derived electrocatalysts; (b) the bar plot of the different types of nitrogen species and their atomic weight percentage; (c) Deconvoluted Zn 2p XPS spectra for ZnMOF derived electrocatalysts.

The atomic concentration of the C 1s region, as derived from XPS analysis, shows an increasing trend with the rising pyrolysis temperature of the samples, which suggests that the amount of carbon-containing species in the material is increasing with higher pyrolysis temperatures. In the ZnMOF-1000 sample, the surface exhibits the highest proportion (94.37%) of atomic carbon (Table 2), suggesting a higher degree of graphitization and leading to improved stability [54]. The specific nitrogen species and their quantities have been identified as crucial factors impacting the oxygen electrocatalytic performance in M-N-C materials, according to multiple studies [55].

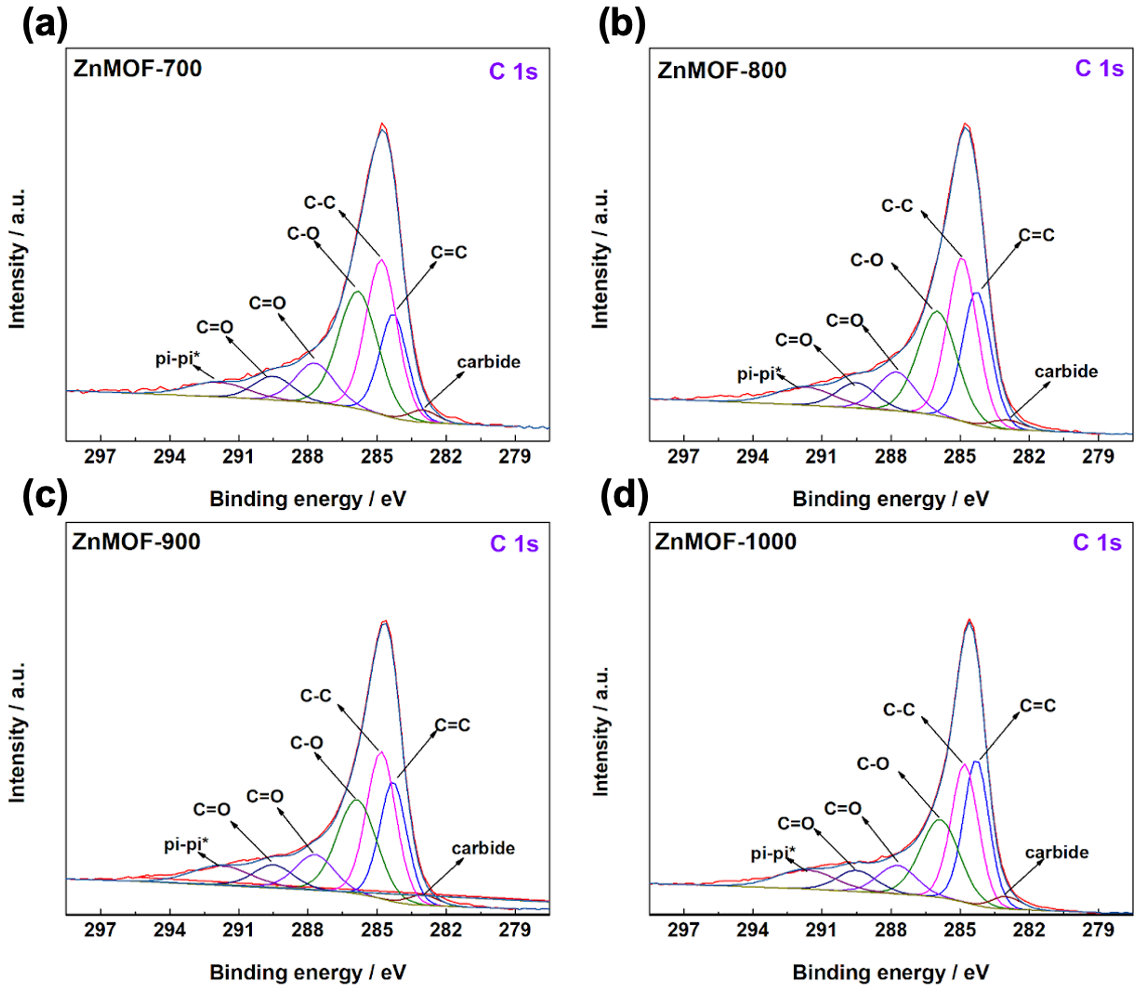

Figure 11. Deconvoluted C 1s XPS spectra for (a) ZnMOF-700, (b) ZnMOF-800, (c) ZnMOF-900, (d) ZnMOF-1000.

The surface properties of the M-N-C materials, including their metal and nitrogen contents, may significantly affect their electrochemical behaviour, particularly when it comes to oxygen electrocatalysis [56]. The overall surface nitrogen content in ZnMOF-700 (15.39 at%) and Zn-MOF-800 (12.82 at%) samples was higher than ZnMOF-900 (8.38 at%) and ZnMOF-1000 (2.96 at%) (Table 2). The observed decrease in nitrogen content in the ZnMOF material with increasing pyrolysis temperature hints at a possible decrease in its catalytic activity. High-resolution N 1s spectra examination showed M-N_x, pyrrolic, pyridinic, imine, and graphitic nitrogen groups (Figure 12). The peak at 398.95, representing M-N_x species, was identified in ZnMOFs pyrolysed at 700, 800, 900, and 1000 °C. These moieties are efficient active sites for the ORR. At 1021.85 and 1025 eV for $2p_{3/2}$ and 1045 eV for $2p_{1/2}$ electronic configurations of Zn atoms, a distinctive feature of the oxidation state of Zn 2p appears, demonstrating a distance of approximately 20 eV (Figure 11 c). Overall, in the

produced Zn-N-C samples, the surface atomic concentration of N 1s and Zn 2p species decreases with an increase in sample heat treatment temperature.

Table 2. Surface elemental composition of Zn-TAL-derived electrocatalysts (at. %) obtained from XPS analysis and bulk Zn composition derived from MP-AES.

Surface elemental composition (at%)						**Bulk metal composition (wt%)**
	C	N	O	Cl	Zn	Zn
ZnMOF-700	68.52	15.39	5.3	1.25	9.53	1.43
ZnMOF-800	76.66	12.82	4.42	0.42	5.68	1.10
ZnMOF-900	85.54	8.38	3.53	0	2.55	0.58
ZnMOF-1000	94.37	2.96	2.22	0	0.44	0.23

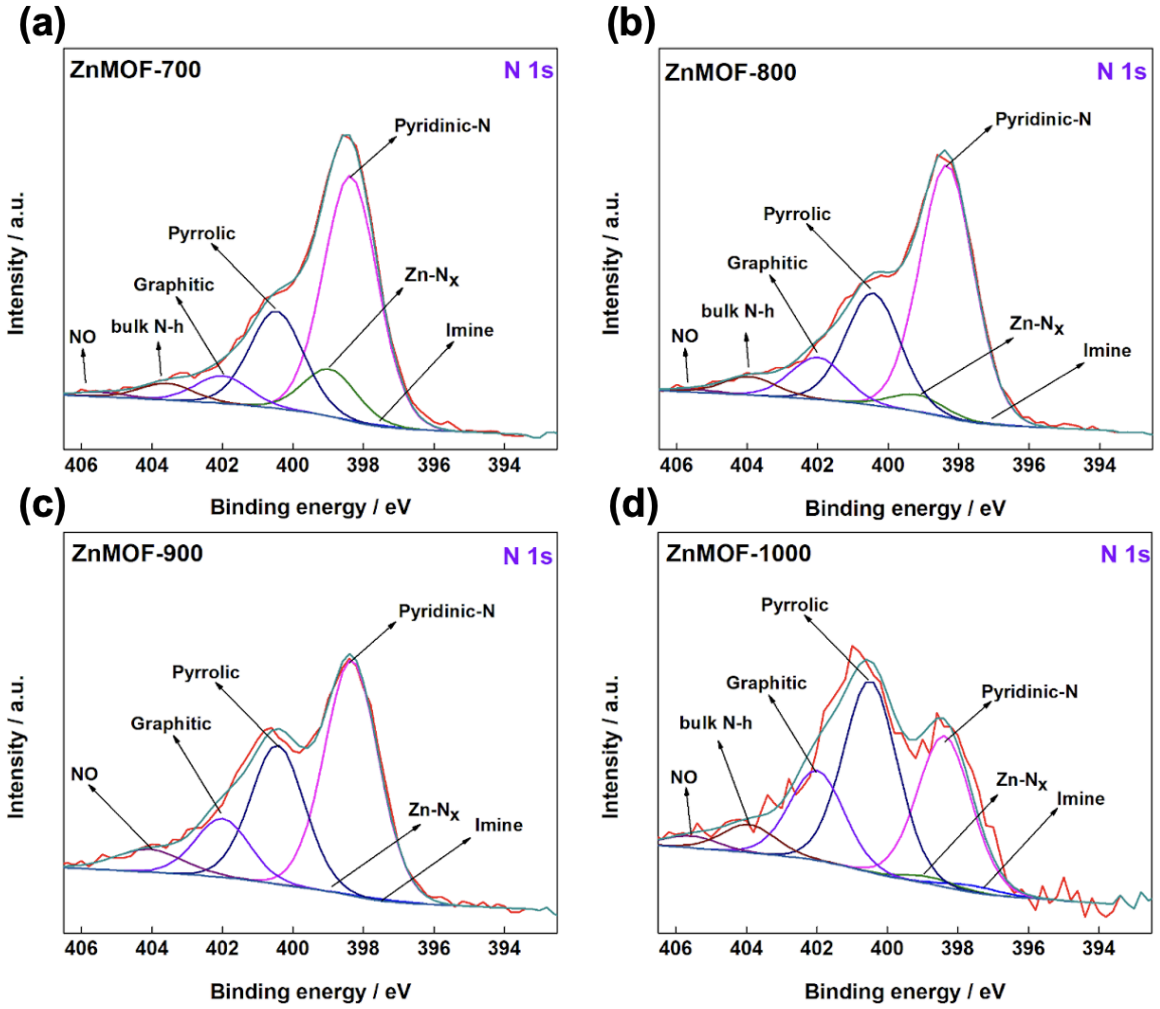

Figure 12. Deconvoluted N 1s XPS spectra for (a) ZnMOF-700, (b) ZnMOF-800, (c) ZnMOF-900, (d) ZnMOF-1000.

4.3. Electrochemical characterisation

4.3.1. Cyclic voltammetry

The ORR behaviour of all four catalysts prepared in this work (ZnMOF-700, ZnMOF-800, ZnMOF-900, ZnMOF-1000) was systematically studied and compared with commercial Pt/C. The electrocatalytic performance of all the above-mentioned samples was initially investigated through cyclic voltammetry (CV) experiments in 0.1 M KOH solution, saturated with both argon and oxygen gases, using a scan rate of 10 mV s^{-1} (Figure 13). All four catalysts showed distinguishable reduction current peaks at ca. +0.80 V vs. RHE in an O_2-saturated electrolyte.

Electrochemically active surface area (ECSA) was calculated from double-layer capacitance (C_{dl}) values, obtained by scanning the catalysts at five different scan rates. Showing that ZnMOF-1000 got the highest value of C_{dl} (Figure 14) indicating a large number of active sites that may boost its ORR catalytic activity.

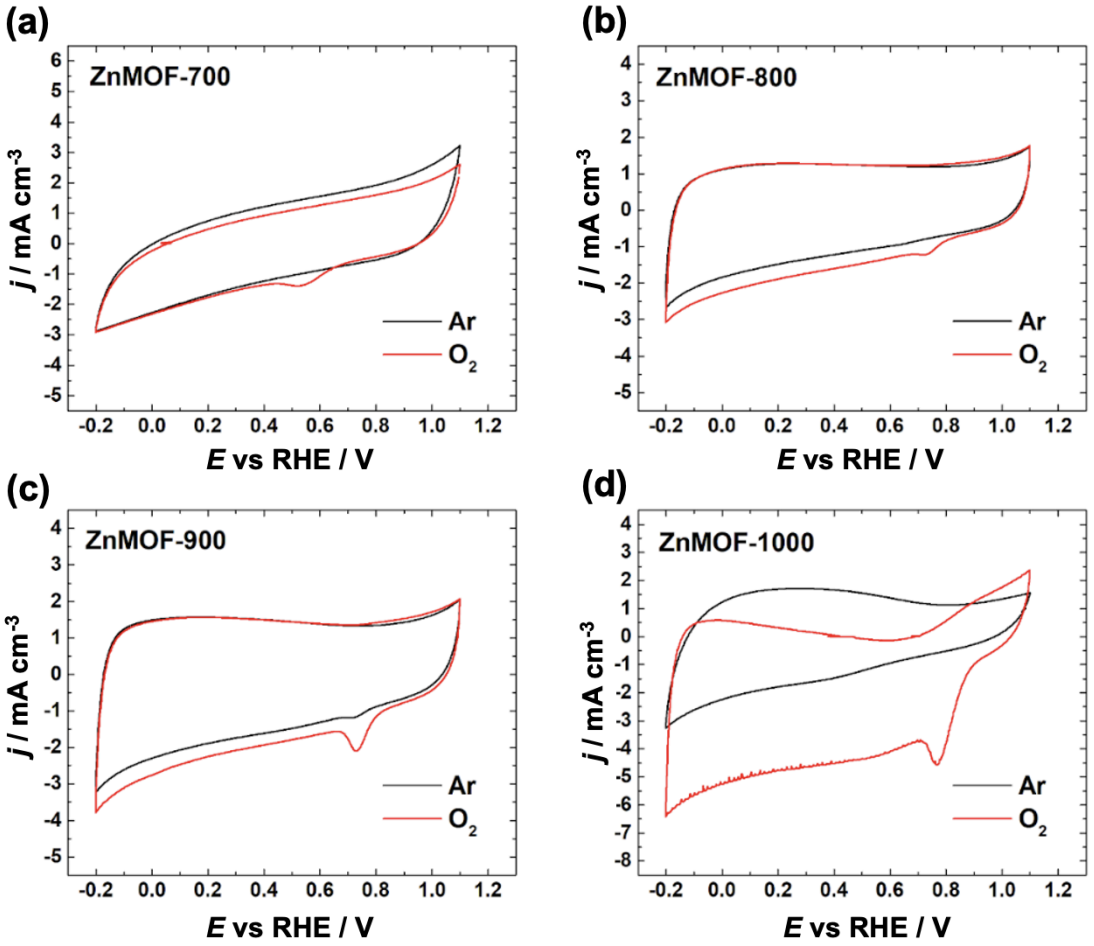

Figure 13. CV curves recorded for (a) ZnMOF-700, (b) ZnMOF-800, (c) ZnMOF-900, and (d) ZnMOF-1000 in Ar- (black line) and O_2-saturated (red line) 0.1 M KOH solution at 10 mV s^{-1}.

To better understand the specific activity of the prepared catalysts, the electrochemically active surface area (ECSA) was evaluated. For this purpose, the samples were subjected to cyclic voltammetry in argon-saturated electrolyte at scan rates of 40, 80, 120, 160 and 200 mV s^{-1}. This allowed the electrochemical capacitance of the double layer (C_{dl}) to be measured (Figure 14).

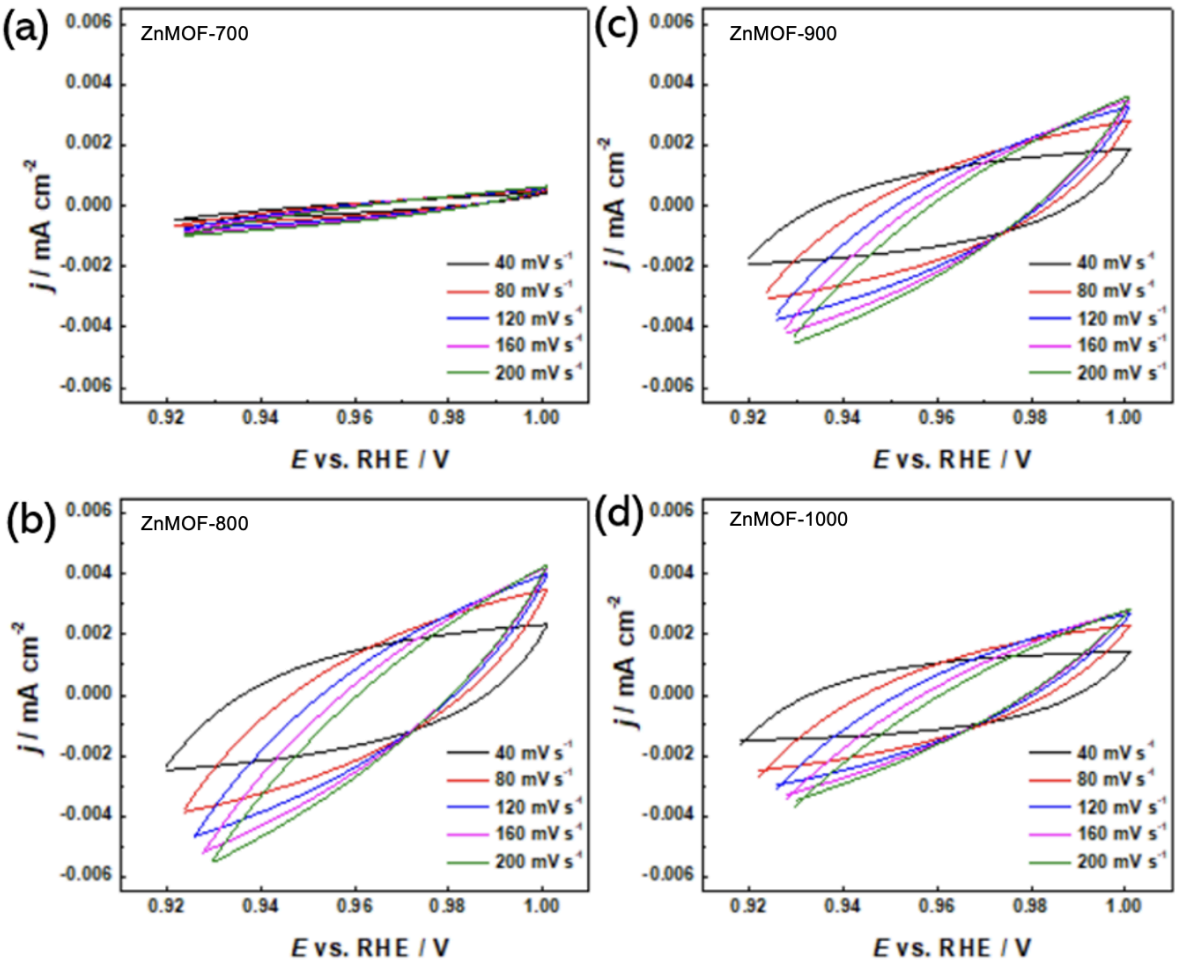

Figure 14. Non-Faradaic CV scans of (a) ZnMOF-700, (b) ZnMOF-800, (c) ZnMOF-900, and (d) ZnMOF-1000 at different scan rates in 0.1 M KOH.

The cathodic and anodic current densities were recorded at non-Faraday potentials, namely in the range of 0.92-1.00 V relative to the reversible hydrogen electrode. The resulting C_{dl} values were plotted as a function of the corresponding scan rates (Figure 15e), with the slope of the approximating trend line representing C_{dl}. The ECSA of the electrocatalysts was calculated using the equation:

$$\text{ECSA} = C_{dl} / C_s,$$

where C_s is the specific capacitance of the electrocatalyst. A C_s value of 0.040 mF cm^{-2} based on known values was used for all MOF materials. Among the synthesized materials, ZnMOF-1000 (57.5 cm^2), followed by ZnMOF-900 (52.5 cm^2), ZnMOF-700 (12.5 cm^2) and ZnMOFL-800 (10 cm^2) showed the largest ECSA. High ECSA of ZnMOF-1000 indicates greater availability of active centers, which may be due to its highly porous structure.

4.3.2. Rotating disk electrode

To evaluate catalyst activity in ORR and a comparison with commercial Pt/C was made using the rotating disc electrode (RDE) method. As shown in Figure 15a, ZnMOF-1000 demonstrated the highest starting potential (E_{on}) of 0.98 V and half-wave potential ($E_{1/2}$) of 0.84 V vs. RHE, only 10 mV lower than Pt/C (0.85 V vs RHE) (Figure 15a). The Tafel slope values obtained from RDE data (Figure 15b) were comparable to Pt/C (61 mV dec^{-1}), indicating improved ORR kinetics in ZnMOF samples.

In addition, ZnMOF-1000 showed a diffusion-limited current density (J_L) of 5.15 mA cm^{-2}, which also confirms its promising catalytic properties. Figure 15c shows the curves obtained by RDE for ZnMOF-1000 at different rotational speeds (ω) from 620 to 2025 rpm. This made it possible to build the Koutecký–Levich (K-L) plots (Figure 15d). The number of electrons transferred per oxygen molecule (n) for ZnMOF-1000 was calculated to be approximately 3.5, which is close to the value 4.0, suggesting that ZnMOF-1000 predominantly follows a four-electron path during ORR.

A full summary of all calculated kinetic parameters for each of the samples studied is given in Table 3. To evaluate the stability of ZnMOF-1000, accelerated testing was performed in an alkaline medium, including 5,000 cycles of potential from +0.6 to +1.0 V RHE at a scanning rate of 50 mV s^{-1} in O_2-saturated electrolyte. Measurements of polarization after stabilization (Figure 15f) confirmed that ZnMOF-1000 retained significant catalytic activity in ORR after prolonged potential cycling, indicating resistance to electrochemical degradation under these test conditions.

Finally, high activity ZnMOF-1000 in the ORR reaction is due to a combination of factors such as nitrogen introduction into the carbon matrix and the presence of atomic distributed zinc, which enhances the internal reaction capacity for ORR. The hierarchical porosity, large specific surface area and large pore volume of ZnMOF-1000 material ensure the availability of active centers and improve mass transport during ORR.

Table 3. Main electrokinetic parameters obtained for Zn-N-C and Pt/C samples.

Electrocatalyst	**$E_{1/2}$ (V vs. RHE)**	**E_{on} (V vs. RHE)**	***n***	**Tafel slope (mV dec^{-1})**	**C_{dl} (mF cm^{-2})**	**ECSA (cm^2)**
ZnMOF-700	0.64	0.76	1.12	-64	0.5	12.5
ZnMOF-800	0.73	0.82	2.37	-53	0.4	10
ZnMOF-900	0.79	0.89	2.46	-51	2.1	52.5
ZnMOF-1000	0.84	0.98	3.45	-53	2.3	57.5
Pt/C	0.85	0.98	4.00	-61	N/A	N/A

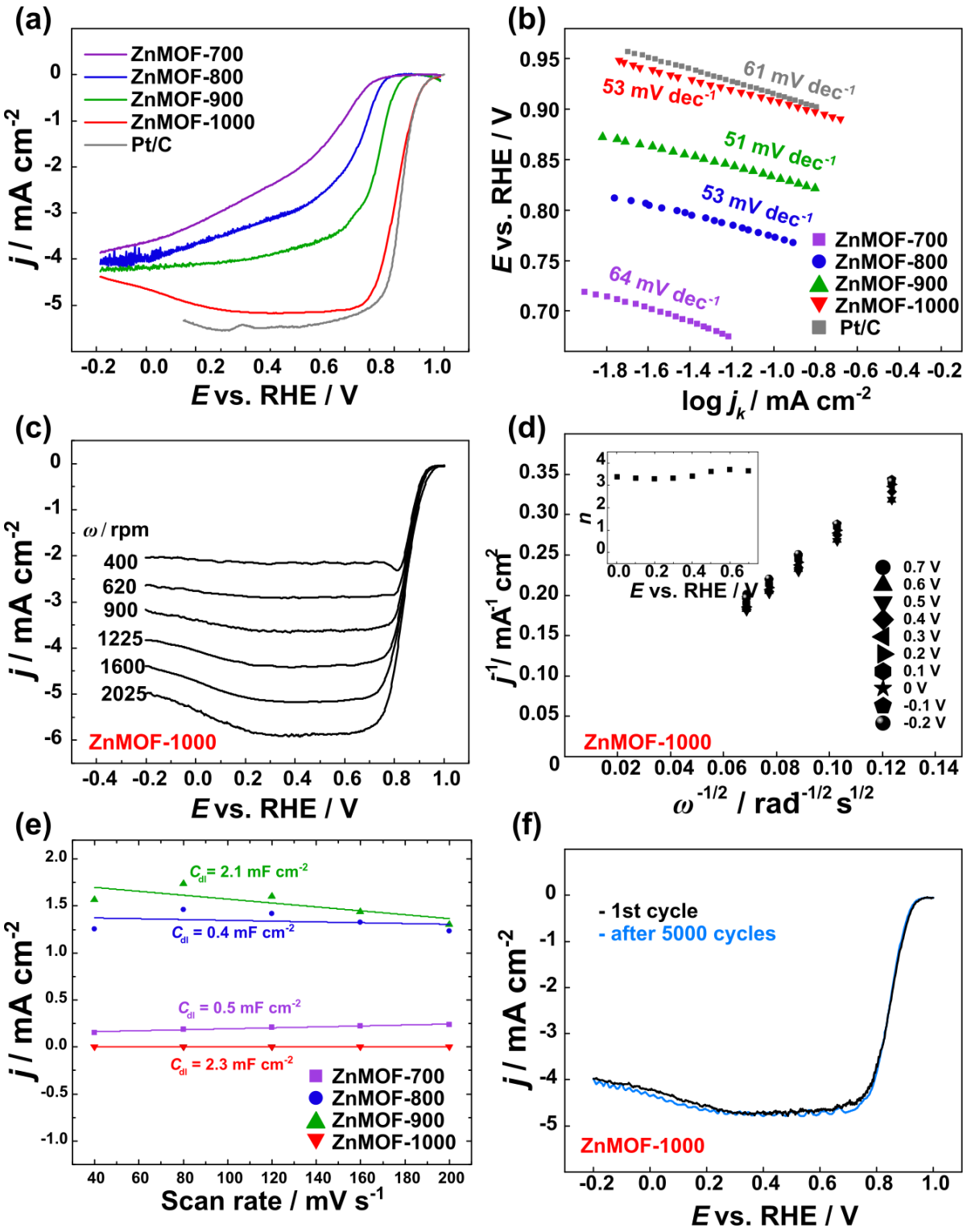

Figure 15. (a) Comparison of ORR polarisation curves recorded for all ZnMOF-derived samples and commercial Pt/C in O_2-saturated 0.1 M KOH at 1600 rpm; (b) ORR Tafel plots derived from the RDE data; (c) ORR polarisation curves recorded for ZnMOF-1000 at different electrode rotation rates; (d) K–L plots constructed from RDE data on ZnMOF-1000 (Inset: number of electrons transferred (n)); (e) the charging current densities plotted against the scan rates for all studied ZnMOF samples; (f) ORR polarisation curves recorded for

ZnMOF-100 before and after 5000 cycles from 0.6 to 1.0 V vs. RHE in O_2-saturated KOH, 10 mV s^{-1}, ω = 1600 rpm.

4.3.3. Anion Exchange Membrane Fuel Cell test

Tests on the ZnMOF-1000 cathode electrocatalyst in an AEMFC at 60 °C (Figure 16) showed a peak power density of 553 mW cm^{-2} and a limiting current density of ~1500 mA cm^{-2} when paired with a PtRu/C anode. These results indicate that ZnMOF-1000 improves AEMFC performance and deserves further investigation for energy conversion applications.

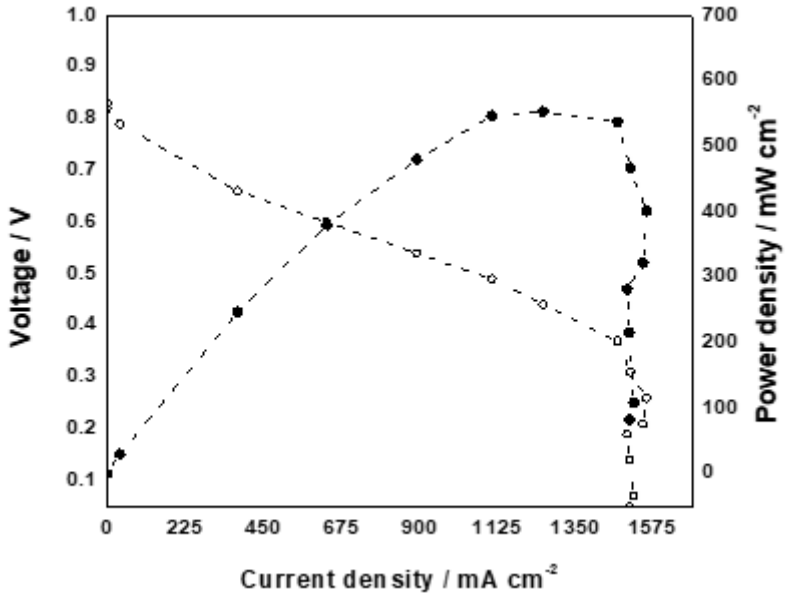

Figure 16. Polarisation curve (empty symbols, Y1 axis) and power density curve (filled symbols, Y2 axis) of an H_2-O_2 AEMFC with ZnMOF-1000 ORR cathode electrocatalyst. Test conditions: cathode and anode loadings of 1 $mg_{ZnMOF-1000}$ cm^{-2} and 0.6 mg_{PtRu} cm^{-2}, respectively, with an HDPE-based AEM. Cell temperature of 60 °C, cathode humidifier temperature of 56 °C and anode humidifier temperature of 54 °C and for O_2 and H_2, respectively, with flow rates of 1 SLPM and back-pressure of 100 kPag for both electrodes.

SUMMARY

Optimised pyrolysis of Zn-TAL yielded a highly efficient Zn-N-C electrocatalyst with preservation of the porous hollow structure. SEM and XRD confirmed the stability of the structure at high temperatures without the formation of Zn aggregates. Electrochemical tests such as cyclic voltammetry and rotating disk electrode measurements showed that ZnMOF-1000 has an onset potential of 0.98 V and a half-wave potential of 0.84 V, comparable to commercial Pt/C. Rotating disk electrode (RDE) studies showed that ZnMOF-1000 preferentially performs a four-electron oxygen reduction (ORR) process with an electron transfer number of 3.45. The material showed high electrochemical stability, retaining significant ORR activity after 5000 cycles in an alkaline medium. In the anion exchange membrane fuel cell (AEMFC), ZnMOF-1000 achieved a peak power density of 553 mW cm^{-2} at 60 °C. This study demonstrates the promise of a low-cost and efficient platinum-free Zn-N-C electrocatalyst derived from Zn-TAL for fuel cells. The versatile precursor Zn-TAL, due to its unique hollow spherical structure and high carbon and nitrogen content, provides efficient transition metal incorporation, improving the performance of electrochemical devices, including metal-air batteries and fuel cells.

REFERENCES

1. Recent development of hydrogen and fuel cell technologies: A review. L. Fan, Z. Tu, S.H. Chan, *Energy Rep.*, 7 (2021) 8421–8446.
2. Advances in stationary and portable fuel cell applications. T. Wilberforce, A. Alaswad, A. Palumbo, M. Dassisti, A.G. Olabi, *Int. J. Hydrog. Energy*, 41 (2016) 16509–16522.
3. Rising Again: Opportunities and Challenges for Platinum-Free Electrocatalysts. M.A. Abbas, J.H. Bang, *Chem. Mater.*, 27 (2015) 7218–7235.
4. Origin of the Overpotential for Oxygen Reduction at a Fuel-Cell Cathode. J.K. Nørskov, J. Rossmeisl, A. Logadottir, L. Lindqvist, J.R. Kitchin, T. Bligaard, H. Jónsson, *J. Phys. Chem. B*, 108 (2004) 17886–17892.
5. The problem with platinum. C. Sealy, *Mater. Today*, 11 (2008) 65–68.
6. Recent advances in active sites identification and new M−N−C catalysts development towards ORR. M. Xu, J. Ge, C. Liu, W. Xing, *J. Phys. Mater.*, 4 (2021) 044008.
7. MOF-Based Co and Mn Embedded in Nitrogen-Doped Microporous Carbon as an Efficient Catalyst for Oxygen Reduction Reaction in Anion Exchange Membrane Fuel Cell. W. Luo, L. Cao, M. Hou, Y. Zhou, Z. Ren, J. Geng, Z. Shao, *Int. J. Energy Res.*, 2023 (2023) 9148994.
8. Construction of highly stable and efficient Zn-based catalyst via Mg modification for propane dehydrogenation. J. Zhang, T. Yu, J. He, J. Chen, G. Wang, Z. Shi, F. Yang, J. Zhao, R. Zhuo, R. Wang, *Mol. Catal.*, 553 (2024) 113717.
9. Hydrogen Fuel Cell Vehicles: Opportunities and Challenges. Q. Hassan, I.D.J. Azzawi, A.Z. Sameen, H.M. Salman, *Sustainability*, 15 (2023) 11501.
10. Recent development of hydrogen and fuel cell technologies: A review. L. Fan, Z. Tu, S.H. Chan, *Energy Rep.*, 7 (2021) 8421–8446.
11. A review of energy storage types, applications and recent developments. S. Koohi-Fayegh, M.A. Rosen, *J. Energy Storage*, 27 (2020) 101047.
12. The development of fuel cell electric vehicles – A review. M. Muthukumar, N. Rengarajan, B. Velliyangiri, M.A. Omprakas, C.B. Rohit, U. Kartheek Raja, *Mater. Today Proc.*, 45 (2021) 1181–1187.
13. Recent advancement and assessment of green hydrogen production technologies. B.S. Zainal, P.J. Ker, H. Mohamed, H.C. Ong, I.M.R. Fattah, S.M.A. Rahman, L.D. Nghiem, T.M.I. Mahlia, *Renew. Sustain. Energy Rev.*, 189 (2024) 113941.
14. Hydrogen Fuel Cell Vehicles: Opportunities and Challenges. Q. Hassan, I.D.J. Azzawi, A.Z. Sameen, H.M. Salman, *Sustainability*, 15 (2023) 11501.
15. Advantages and Technological Progress of Hydrogen Fuel Cell Vehicles. T. Mo, Y. Li, Y. Luo, *World Electr. Veh. J.*, 14 (2023) 162.
16. Review of solid oxide fuel cell materials: cathode, anode, and electrolyte. S. Hussain, L. Yangping, *Energy Transit.*, 4 (2020) 113–126.
17. Electrospun Composite Proton-Exchange and Anion-Exchange Membranes for Fuel Cells. Z. Shang, R. Wycisk, P. Pintauro, *Energies*, 14 (2021) 6709.
18. Reverse-Current Decay in Hydroxide Exchange Membrane Fuel Cells. R.B. Kaspar, J.A. Wittkopf, M.D. Woodroof, M.J. Armstrong, Y. Yan, *J. Electrochem. Soc.*, 163 (2016) F377.
19. Review of solid oxide fuel cell materials: cathode, anode, and electrolyte. S. Hussain, L. Yangping, *Energy Transit.*, 4 (2020) 113–126.
20. Review on hydrogen storage materials and methods from an electrochemical viewpoint. M. Kaur, K. Pal, *J. Energy Storage*, 23 (2019) 234–249.
21. Recent advances in metal-organic frameworks derived electrocatalysts for oxygen reduction reaction. S. Wu, X. Qu, J. Zhu, X. Liu, H. Mao, K. Wang, G. Zhou, J. Chi, L.

Wang, *J. Alloys Compd.*, 970 (2024) 172518.
22. Heterogeneous nanocarbon materials for oxygen reduction reaction. D.-W. Wang, D. Su, *Energy Environ. Sci.*, 7 (2014) 576–591.
23. Carbon-based single atom catalysts for tailoring the ORR pathway: a concise review. J. Hu, W. Liu, C. Xin, J. Guo, X. Cheng, J. Wei, C. Hao, G. Zhang, Y. Shi, *J. Mater. Chem. A*, 9 (2021) 24803–24829.
24. Research Progress on Atomically Dispersed Fe-N-C Catalysts for the Oxygen Reduction Reaction. Y. Lian, J. Xu, W. Zhou, Y. Lin, J. Bai, *Molecules*, 29 (2024) 771.
25. Research Progress on Atomically Dispersed Fe-N-C Catalysts for the Oxygen Reduction Reaction. Y. Lian, J. Xu, W. Zhou, Y. Lin, J. Bai, *Molecules*, 29 (2024) 771.
26. A family of Fe-N-C oxygen reduction electrocatalysts for microbial fuel cell (MFC) application: Relationships between surface chemistry and performances. C. Santoro, A. Serov, R. Gokhale, S. Rojas-Carbonell, L. Stariha, J. Gordon, K. Artyushkova, P. Atanassov, *Appl. Catal. B Environ.*, 205 (2017) 24–33.
27. Insight into the active sites of M–N–C single-atom catalysts for electrochemical CO2 reduction. Q. Pan, Y. Chen, S. Jiang, X. Cui, G. Ma, T. Ma, *EnergyChem*, 5 (2023) 100114.
28. Enhancing the Stability of a Pt-Free ORR Catalyst via Reaction Intermediates. N. Helsel, P. Choudhury, *Adv. Mater. Interfaces*, 10 (2023) 2202132.
29. The role of nanostructure in nitrogen-containing carbon catalysts for the oxygen reduction reaction. P.H. Matter, L. Zhang, U.S. Ozkan, *J. Catal.*, 239 (2006) 83–96.
30. Different types of nitrogen species in nitrogen-doped carbon material: The formation mechanism and catalytic role on oxygen reduction reaction. Z. Huang, Z. Liao, W. Yang, H. Zhou, C. Fu, Y. Gong, L. Chen, Y. Kuang, *Electrochimica Acta*, 245 (2017) 957–966.
31. Unraveling the mechanism of ligands regulating electronic structure of MN4 sites with optimized ORR catalytic performance. B. Li, H. Xie, C. Yang, C. Shi, C. He, N. Zhao, E. Liu, *Appl. Surf. Sci.*, 595 (2022) 153526.
32. B. Li, H. Xie, C. Yang, C. Shi, C. He, N. Zhao, E. Liu, *Appl. Surf. Sci.*, 595 (2022) 153526.
33. Transition Metal–Nitrogen–Carbon (M–N–C) Catalysts for Oxygen Reduction Reaction. Insights on Synthesis and Performance in Polymer Electrolyte Fuel Cells. L. Osmieri, *ChemEngineering*, 3 (2019) 16.
34. Multifunctional Electrocatalysis on Single-Site Metal Catalysts: A Computational Perspective. R. Cepitis, N. Kongi, V. Grozovski, V. Ivaništšev, E. Lust, *Catalysts*, 11 (2021) 1165.
35. Recent advances in metal-organic frameworks-derived carbon-based electrocatalysts for the oxygen reduction reaction. C. Yang, X. Ma, J. Zhou, Y. Zhao, X. Xiang, H. Shang, B. Zhang, *Int. J. Hydrog. Energy*, 47 (2022) 21634–21661.
36. Catalysts by pyrolysis: Transforming metal-organic frameworks (MOFs) precursors into metal-nitrogen-carbon (M-N-C) materials. Y. Huang, Y. Chen, M. Xu, A. Ly, A. Gili, E. Murphy, T. Asset, Y. Liu, V. De Andrade, C.U. Segre, A.L. Deriy, F. De Carlo, M. Kunz, A. Gurlo, X. Pan, P. Atanassov, I.V. Zenyuk, *Mater. Today*, 69 (2023) 66–78.
37. Metal–Organic Framework (MOF)-Derived Catalyst for Oxygen Reduction Reaction (ORR) Applications in Fuel Cell Systems: A Review of Current Advancements and Perspectives. K. Dhanabalan, M. Perumalsamy, G. Sriram, N. Murugan, Shalu, T. Sadhasivam, T.H. Oh, *Energies*, 16 (2023) 4950.
38. Metal complexes derived from bidentate ligands: Synthesis, catalytic and biological applications. D.I. Ugwu, J. Conradie, *Inorganica Chim. Acta*, 553 (2023) 121518.
39. Advances and Applications of Metal-Organic Frameworks (MOFs) in Emerging Technologies: A Comprehensive Review. D. Li, A. Yadav, H. Zhou, K. Roy, P. Thanasekaran, C. Lee, *Glob. Chall.*, 8 (2024) 2300244.

40. Metal–organic frameworks and their catalytic applications. M.S. Alhumaimess, *J. Saudi Chem. Soc.*, 24 (2020) 461–473.
41. MOF-derived Co, Fe, and Ni co-doped N-enriched hollow carbon as efficient electrocatalyst for oxygen reduction reaction. Y. Jing, Y. Cheng, L. Wang, Y. Liu, B. Yu, C. Yang, *Chem. Eng. J.*, 397 (2020) 125539.
42. MOF-derived Co, Fe, and Ni co-doped N-enriched hollow carbon as efficient electrocatalyst for oxygen reduction reaction. Y. Jing, Y. Cheng, L. Wang, Y. Liu, B. Yu, C. Yang, *Chem. Eng. J.*, 397 (2020) 125539.
43. Catalysts by pyrolysis: Transforming metal-organic frameworks (MOFs) precursors into metal-nitrogen-carbon (M-N-C) materials. Y. Huang, Y. Chen, M. Xu, A. Ly, A. Gili, E. Murphy, T. Asset, Y. Liu, V. De Andrade, C.U. Segre, A.L. Deriy, F. De Carlo, M. Kunz, A. Gurlo, X. Pan, P. Atanassov, I.V. Zenyuk, *Mater. Today*, 69 (2023) 66–78.
44. Turning metal-organic frameworks into efficient single-atom catalysts via pyrolysis with a focus on oxygen reduction reaction catalysts. L. Hu, W. Li, L. Wang, B. Wang, *EnergyChem*, 3 (2021) 100056.
45. Mesoporous iron-nitrogen co-doped carbon material as cathode catalyst for the anion exchange membrane fuel cell. J. Lilloja, M. Mooste, E. Kibena-Põldsepp, A. Sarapuu, B. Zulevi, A. Kikas, H.-M. Piirsoo, A. Tamm, V. Kisand, S. Holdcroft, A. Serov, K. Tammeveski, *J. Power Sources Adv.*, 8 (2021) 100052.
46. Effect of water management in membrane and cathode catalyst layers on suppressing the performance hysteresis phenomenon in anion-exchange membrane fuel cells. K. Otsuji, Y. Shirase, T. Asakawa, N. Yokota, K. Nagase, W. Xu, P. Song, S. Wang, D.A. Tryk, K. Kakinuma, J. Inukai, K. Miyatake, M. Uchida, *J. Power Sources*, 522 (2022) 230997.
47. The Role of Ligands in the Chemical Synthesis and Applications of Inorganic Nanoparticles. A. Heuer-Jungemann, N. Feliu, I. Bakaimi, M. Hamaly, A. Alkilany, I. Chakraborty, A. Masood, M.F. Casula, A. Kostopoulou, E. Oh, K. Susumu, M.H. Stewart, I.L. Medintz, E. Stratakis, W.J. Parak, A.G. Kanaras, *Chem. Rev.*, 119 (2019) 4819–4880.
48. Fused Hybrid Linkers for Metal–Organic Framework-Derived Bifunctional Oxygen Electrocatalysts. K. Ping, A. Braschinsky, M. Alam, R. Bhadoria, V. Mikli, A. Mere, J. Aruväli, P. Paiste, S. Vlassov, M. Kook, M. Rähn, V. Sammelselg, K. Tammeveski, N. Kongi, P. Starkov, *ACS Appl. Energy Mater.*, 3 (2020) 152–157.
49. Theoretical analysis of single Zn atoms with N/C on graphene promoting oxygen redox in alkaline medium. L. Jin, K. Wu, M. Liao, D. Wang, B. Jayaraman, S.G. Peera, C. Liu, *Mol. Catal.*, 553 (2024) 113799.
50. Catalysts by pyrolysis: Transforming metal-organic frameworks (MOFs) precursors into metal-nitrogen-carbon (M-N-C) materials. Y. Huang, Y. Chen, M. Xu, A. Ly, A. Gili, E. Murphy, T. Asset, Y. Liu, V. De Andrade, C.U. Segre, A.L. Deriy, F. De Carlo, M. Kunz, A. Gurlo, X. Pan, P. Atanassov, I.V. Zenyuk, *Mater. Today*, 69 (2023) 66–78.
51. Y. Huang, Y. Chen, M. Xu, A. Ly, A. Gili, E. Murphy, T. Asset, Y. Liu, V. De Andrade, C.U. Segre, A.L. Deriy, F. De Carlo, M. Kunz, A. Gurlo, X. Pan, P. Atanassov, I.V. Zenyuk, *Mater. Today*, 69 (2023) 66–78.
52. Catalysts by pyrolysis: Transforming metal-organic frameworks (MOFs) precursors into metal-nitrogen-carbon (M-N-C) materials. Y. Huang, Y. Chen, M. Xu, A. Ly, A. Gili, E. Murphy, T. Asset, Y. Liu, V. De Andrade, C.U. Segre, A.L. Deriy, F. De Carlo, M. Kunz, A. Gurlo, X. Pan, P. Atanassov, I.V. Zenyuk, *Mater. Today*, 69 (2023) 66–78.
53. Recent progress of M-N-C single atom electrocatalysts for carbon dioxide reduction reaction. A. Fauzi, X. Chen, H. Zhao, S. Cao, L. Kong, S. Huang, S. Zhang, X. Ma, *Energy*, 1 (2023) 100045.
54. Atomically precise electrocatalysts for oxygen reduction reaction. L. Yan, P. Li, Q. Zhu, A. Kumar, K. Sun, S. Tian, X. Sun, *Chem*, 9 (2023) 280–342.
55. Exploring the nitrogen species of nitrogen doped graphene as electrocatalysts for oxygen

reduction reaction in Al–air batteries. Y. Liu, J. Li, W. Li, Y. Li, F. Zhan, H. Tang, Q. Chen, *Int. J. Hydrog. Energy*, 41 (2016) 10354–10365.
56. Effect of surface characteristics of carbon host on electrochemical performance of nonaqueous Li–O2 batteries. M. Lee, Y. Yoo, J.H. Kwak, Y.S. Yun, H.-G. Jung, D. Byun, S.H. Oh, H.-D. Lim, *Chem. Eng. J.*, 412 (2021) 128549.

NON-EXCLUSIVE LICENCE TO REPRODUCE THESIS AND MAKE THESIS PUBLIC

I, Jekaterina Pozdnyakova,

1. herewith grant the University of Tartu a free permit (non-exclusive licence) to

reproduce, for the purpose of preservation, including for adding to the DSpace digital archives until the expiry of the term of copyright,

"Pyrolytic Metamorphosis of Zn-TAL MOF into Highly Active Nitrogen-Doped Carbon Catalyst for Oxygen Reduction Reaction"

supervised by Dr. Akmal Kosimov, Dr. Nadezda Kongi

2. I grant the University of Tartu a permit to make the work specified in p. 1 available to the public via the web environment of the University of Tartu, including via the DSpace digital archives, under the Creative Commons licence CC BY NC ND 3.0, which allows, by giving appropriate credit to the author, to reproduce, distribute the work and communicate it to the public, and prohibits the creation of derivative works and any commercial use of the work until the expiry of the term of copyright.

3. I am aware of the fact that the author retains the rights specified in p. 1 and 2.

4. I certify that granting the non-exclusive licence does not infringe other persons' intellectual property rights or rights arising from the personal data protection legislation.

Ekaterina Pozdnyakova

20.05.2025